Journal of the Mechanics and Physics of Solids 143 (2020) 104028

Contents lists available at ScienceDirect

Journal of the Mechanics and Physics of Solids

journal homepage: www.elsevier.com/locate/jmps

Rate-dependent fracture of transient networks

Tong Shen, Franck J. Vernerey*

Department of Mechanical Engineering, Program of Materials Science and Engineering, University of Colorado, Boulder USA

ARTICLE INFO

Article history:
Received 13 March 2020
Revised 19 May 2020
Accepted 19 May 2020
Available online 13 June 2020

Keywords:
Rate-dependent fracture
Viscoelasticity
Crack driving force
Finite element analysis
Transient networks

ABSTRACT

Soft viscoelastic polymers and gels are commonly used a wide range of applications owing to their softness and the ability to accommodate large deformations. Their applicability is however often limited by their tendency to fracture in ways that are cannot be predicted by conventional elastic fracture mechanics. Our understanding of fracture in this class of solid has particularly been hindered by the incapacity of determining the competition viscous flow and fracture under finite strains. To tackle this problem, this paper presents a framework that quantitatively captures the interplay between energy dissipation and crack propagation in soft solids made of a single transient network. Using a combined analytical and numerical study, we investigate the dynamics of crack propagation at various loading rates and for networks that display different sensitivities to force. Our results point out to four different crack characteristic behaviors, for which we unveiled the respective mechanisms, all involving a strong interplay between chain deformation, bond dynamics and rupture.

1. Introduction

Soft polymeric materials that are resistant to fracture are highly desirable in a wide range of existing and emerging applications including adhesives (Creton and Ciccotti, 2016), soft robotics (Coyle et al., 2018), tissue engineering (Akalp et al., 2016; Bryant and Vernerey, 2018; Haque et al., 2012) and stretchable electronics (Lin et al., 2016). In practice, macroscopic fracture usually originates from the catastrophic growth of small defects that leads to the damage of surrounding material. One general metric to characterize a material's resistance to fracture is the fracture toughness $\mathcal{G}$, defined as the energy required to advance the crack by a unit area (Long et al., 2014). To improve the applicability of soft polymeric materials in applications, tremendous effort has been devoted in the past decade to enhancing $\mathcal{G}$ through a variety of strategies, including particle-reinforcement (Agrawal et al., 2013; Moutos et al., 2007), sacrificial bond breaking (Gong et al., 2003; Haque et al., 2012; Millereau et al., 2018), and inducing viscoelasticity by transient reversible networks (Mayumi et al., 2016; Sun et al., 2012; 2013; Wu et al., 2017). A thorough review of toughening strategies and mechanisms can be found in Zhao (2014). Despite differences in methodology, a common object of these works is to introduce a bulk energy dissipation mechanism to shield the defects from the energy inflow by external loading (Creton and Ciccotti, 2016; Zhao, 2014). Among these strategies, the introduction of a transient network has been favored by many researchers due to the capability of bond reformation (Ihsan et al., 2013; Zhang et al., 2016). This leads to advantageous characteristics of recovering the mechanical

* Corresponding author.
E-mail address: franck.vernerey@colorado.edu (F.J. Vernerey).

https://doi.org/10.1016/j.jmps.2020.104028
0022-5096/

strength after large deformation and self-healing after cutting (Wu et al., 2017). In addition, with the increasing capacity of controlling the bond structure at the molecular level, it is possible to tune the bond dynamics towards desired mechanical behaviors.

While many articles report the fabrication of novel transient networks with high fracture resistance, our theoretical understanding remains limited (Long and Hui, 2016; Long et al., 2020). The main difficulty lies in an accurate description of material's viscoelastic behavior arising from bond dynamics at finite strain. Earlier theoretical studies can be dated back to the 1960s', starting from Williams (1968), Knauss (1966, 1970, 2015) and Schapery (1975, 1984). These works employed the cohesive approach and assumed a linear-viscoelastic material behavior in the cohesive zone. In an alternative approach, Christensen (1979) incorporated the role of viscous dissipation into a generalized Griffith's energy-based criterion to predict the crack propagation in a viscoelastic strip. Hui et al. (1992) later obtained a similar expression for the crack driving force as Christensen at the limit of very large velocity via a rate-dependent cohesive zone analysis of crack propagation. At the level of qualitative understanding, De Gennes (1996) employed scaling analysis and physical arguments and proposed a theoretical picture, the Viscoelastic Trumpet Model, describing the effect of viscous dissipation on the material behavior near a propagating crack tip. Considering the interplay between material deformation and relaxation, de Gennes suggested that a steadily moving crack tip in the viscoelastic medium is wrapped by an unrelaxed elastic zone and a viscous dissipation zone (Saulnier et al., 2004; Tabuteau et al., 2011). The crack takes a different profile in these two regimes and collectively its shape is similar to a trumpet profile.

While the above studies are based on linear, small deformation viscoelasticity, in practice, these materials usually experience large strains and exhibit highly nonlinear viscoelastic behaviors especially near the crack tip. Although several nonlinear viscoelastic models have been proposed in the literature (Bergström and Boyce, 1998; Long et al., 2014; Mao et al., 2017; Vernerey and Long, 2017), there were no studies on the viscoelastic fracture at finite strain until the recent serial work of Guo et al. (2019, 2018); Hui et al. (2019), where the time-dependent stress fields near a static crack tip were evaluated. This approach has however not been used to evaluate the bulk dissipation and the crack driving force. One major barrier is that this model relies on the convolutional integration over the deformation history at each material point, which is computationally challenging when solving for a full field problem with complicated geometry and loading. This issue can be addressed by using the transient network theory (TNT) (Tanaka and Edwards, 1992; Tobolsky and Eyring, 1943; Yamamoto, 1956) that derives the macroscopic mechanics based on the statistical description of chain configuration and dynamics at the microscopic level. One advantage is that this theory is derived in a time-incremental format based on evolution equations, which bypasses the need for convolutional integral when evaluating the elastic stored energy density and dissipation. In a recent effort, Vernerey and Long (2017); Vernerey (2018) introduced new forms of this theory that characterize the chain statistical distribution via an average measure, the conformation tensor. This largely simplifies the framework and makes it convenient for computational implementation. In later efforts, this theory has been implemented into a coupled Eulerian-Lagrange finite element framework that simulates the rate dependent response of soft synthetic and biological materials at very large deformations (Shen et al., 2019a; 2019b; Vernerey et al., 2018b), which shows its potential for the study on the fracture of soft viscoelastic materials. Supposing that the crack driving force is obtained, its relationship to crack stability needs to be determined based on the mechanism of chain rupture at the tip. The conventional model, the Lake-Thomas theory (Lake and Thomas, 1967), proposes a rate-independent framework that relates the chain rupture to a critical stretch level. However, this theory was contradicted by several experiments that indicates chain damage is associated with the rate at which they are stretched (Gent, 1996; Ghatak et al., 2000). Alternatively, Chaudhury (1999); Hui et al. (2004) proposed that this rate-dependent rupture is related to thermally activated kinetic process of the chains at the tip, where bond dissociation is accelerated due to the local amplified chain stretch. Based on this consideration, a crack driving force - velocity relationship was derived based on a rate equation of bond kinetic and has qualitatively explained experimental measurements (Ghatak et al., 2000). However, since this model only focuses on microscopic events at the tip, it needs to be incorporated with a continuum model to account for the effect of bulk dissipation.

Our objective here is to develop a model that is the physically simplest possible of a transient network, that could in time provide a stepping stone to explore more complex situations. The network is therefore assumed to have a uniform mesh size, with a dynamic that is governed by a unique time scale: that of the bond association and dissociation. We neglect additional toughening mechanisms occurring at the crack tip (van der Kooij et al., 2018; Long et al., 2020), and thus only concentrate on the so-called quasi-brittle transient networks (Ligoure and Mora, 2013; Shabbir et al., 2016; Tabuteau et al., 2011; 2009) where a crack only consumes energy by creating new surfaces. The following presentation could of course include a variety of more complex processes including additional rate dependent processes arising from the polymer-solvent interactions (Dhote and Vernerey, 2014; Wang and Hong, 2012), chain reptation through entanglements (De Gennes, 1976; Lalitha Sridhar and Vernerey, 2018), multiple bond kinetics (Sun et al., 2012) or chain stiffening (Lavoie et al., 2016; Vernerey et al., 2018a), but all of these would be at great expense of the exposition. Instead, we focus here on exploring the non-intuitive phenomena that would arise from this simple class of quasi-brittle dynamics networks. To achieve this, we employ the transient network theory (TNT) at the macroscopic level to determine the crack driving force taking into account for the viscous dissipation. At the crack tip, we employ the cohesive zone model that relates the crack driving force to crack stability and velocity developed by Chaudhury (1999). The structure of the paper is as follows. Section 2 investigates rate dependent response of material made of transient networks and calculates the crack driving force based on the interplay between external load and viscous dissipation. We also investigate the role of viscous dissipation in fracture through a simplified fracture case. Section 3 then introduces a general numerical approach to examine the crack stability at large

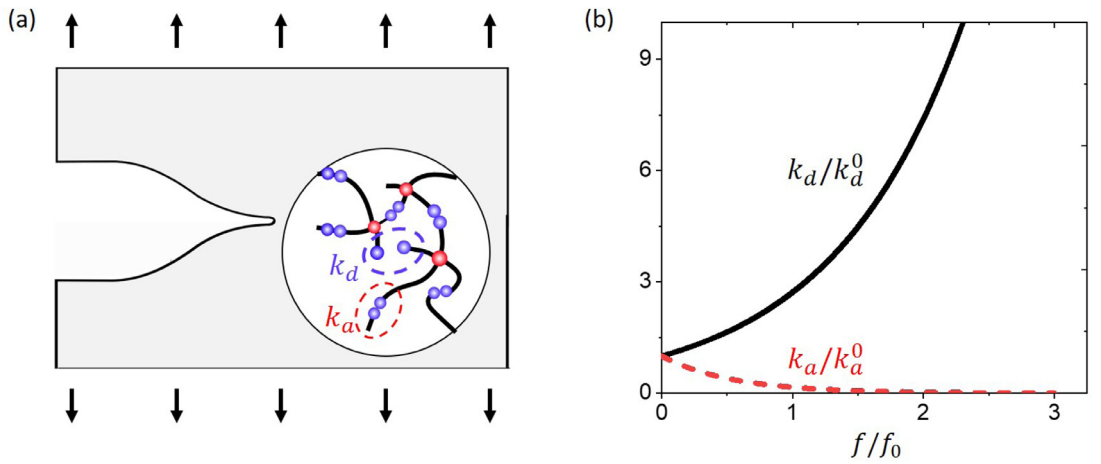

Fig. 1. (a) A schematic of fracture test of a material made of transient networks. (b) The change of bond association rate k_a and dissociation rate k_d as functions of force.

deformation. This framework also relates the crack velocity to crack tip driving force based on the work of Chaudhury (1999). Section 4 finally explores the material behavior under pure shear fracture test at different loading conditions.

2. Viscous dissipation and crack driving force

The mechanical response of viscoelastic solids is usually more complicated than their elastic counterparts due to their capacity of dissipating energy during loading and rate dependency. In this paper, we focus our study on solids made of "transient" polymer networks, characterized by non-covalent crosslinks. In these networks, crosslinks can dissociate and reassociate under external stimuli or thermal fluctuation, leading to network reorganization over time. Some example of these solids are polymers with covalent adaptable bonds (Kloxin and Bowman, 2013) or physical bonds such as hydrogen bonds (Li et al., 2007) and ionic interactions (Sun et al., 2013). It is usually considered that an associated chain can dissociate at any state, but a free chain can only reassociate at its stress free state (Vernerey and Long, 2017). Therefore, the stored elastic energy is dissipated through the dissociation process. In the following, we will explore the response of this network first during uniform extension and then during fracture experiments.

2.1. Flow and elasticity of transient networks

The dynamics of bonds in a transient network is usually characterized by the rate of bond association k_a and the rate of dissociation k_d, respectively (Fig. 1a). According to Erying's theory (Krausz, 1976; Tobolsky and Eyring, 1943), the magnitudes of k_a and k_d depend on the standard energy barrier for association (ΔG^a) and dissociation (ΔG^d), and the force f carried by the chain. Since a detailed analysis is already given in Krausz (1976); Yu et al. (2018), we directly take the expression of k_a and k_d as $k_a = \nu exp(-\frac{\Delta G^a + f\lambda}{k_B T})$ and $k_d = \nu exp(-\frac{\Delta G^d - f\lambda}{k_B T})$ where ν is the natural thermal vibration frequency, $k_B T$ is the thermal energy and λ is a activation length for bond dynamics. To obtain a simpler form, let us further introduce the force-free rates of bond dynamics $k_a^0 = \nu exp(-\frac{\Delta G^a}{kT})$ and $k_d^0 = \nu exp(-\frac{\Delta G^d}{k_B T})$ and obtain:

$$k_a = k_a^0 exp\left(-\frac{f}{f_0}\right) \quad \text{and} \quad k_d = k_d^0 exp\left(\frac{f}{f_0}\right) \tag{1}$$

where $f_0 = k_B T/\lambda$ measures the force sensitivity of k_a and k_d (i.e., a larger f_0 indicates a weak force sensitivity). Fig. 1b illustrates the changes of k_a and k_d as functions of force. For the convenience of analysis, it is usually assumed that k_a, k_d are constant when the chain stretch is small compared to their contour length (Sun et al., 2017). This assumption has been validated in several experiments where the material's relaxation time is almost invariant of stretch level in a certain range (Mayumi et al., 2013; Narita et al., 2013; Pellens et al., 2004). When chains are highly stretched, i.e., near their contour length, this assumption fails and force sensitivity must be considered. In the context of fracture, amplification of chain stretch usually occurs in a small region near the crack tip. Therefore, in this work, we assume that k_a, k_d are constants in the specimen except for a small region near the crack tip.

Due to bond dynamics, only a fraction of chains are connected in the network and contribute to its elasticity. Considering that chain dynamics follow first order kinetics, the concentration n of connected chains can be determined at any time by solving the evolution equation (Vernerey and Long, 2017):

$$\frac{dn}{dt} = k_a(n_t - n) - k_d n \tag{2}$$

where n_t is the total concentration of chains in the network. At chemical equilibrium state ($dn/dt = 0$), the concentration of connected chains becomes a constant and can be found as $n = n_t k_a/(k_a + k_d)$. The elastic deformation of the network may then be connected to the stretch ratio λ of connected chains via the conformation tensor (Vernerey and Long, 2017; Vernerey, 2018):

$$\boldsymbol{\mu} = \langle \boldsymbol{\lambda} \otimes \boldsymbol{\lambda} \rangle \tag{3}$$

where the operator $\langle \cdot \rangle$ represents the average operation over the chain configuration space (Vernerey, 2018) and $\boldsymbol{\lambda} = \mathbf{r}/r_0$ where $\mathbf{r}$ is a chain's end-to-end vector and $r_0 = \sqrt{N}b$ the average length of a chain in its stress free configuration. With this definition, the conformation tensor $\boldsymbol{\mu}$ is equal to the identity tensor $\mathbf{I}$ when the network is stress-free. However, upon deformation, $\boldsymbol{\mu}$ changes in time due to a competition between chain stretch and bond dynamics. If we assume that k_a and k_d are constants, one can show taht the conformation tensor evolves according to Vernerey and Long (2017) (detailed derivation is given in Appendix A):

$$\dot{\boldsymbol{\mu}} = \mathbf{L}\boldsymbol{\mu} + \boldsymbol{\mu}^T\mathbf{L}^T + k_d(\mathbf{I} - \boldsymbol{\mu}) \tag{4}$$

where $\mathbf{L} = \dot{\mathbf{F}}\mathbf{F}^{-1}$ is the velocity gradient experienced by the network ($\mathbf{F}$ being the deformation gradient) and $\boldsymbol{\mu}_0 = 3/tr(\boldsymbol{\mu}^{-1})I$ is the state for reassociation. We note that the chemical equilibrium condition $n = n_t k_a/(k_a + k_d)$ and affined deformation $\dot{\boldsymbol{\lambda}} = \mathbf{L}\boldsymbol{\lambda}$ were assumed to obtain the above equation. The first two terms on the right hand side describe the contribution from macroscopic deformation while the latter two terms account for the dissociation of connected chains at the current state ($\boldsymbol{\mu}$) and the association of free chains in a uniformed state ($3/tr(\boldsymbol{\mu}^{-1})\mathbf{I}$). We note that this is a stressed state due to the incompressibility of the network. For a purely elastic network (i.e. $k_a = k_d = 0$) Eq. (4) degenerates to the rate of the Finger deformation tensor $\dot{\boldsymbol{\mu}} = \mathbf{L}\boldsymbol{\mu} + \boldsymbol{\mu}^T\mathbf{L}^T$ (Holzapfel, 2000). Since $\boldsymbol{\mu}$ characterizes the elastic deformation of the network, it is directly connected to the elastic energy Ψ and rate of energy dissipation $\mathcal{D}$. Assuming Gaussian chain statistics (i.e., the force-stretch relation of a chain is linear), these two quantities are defined as Vernerey and Long (2017):

$$\Psi = \frac{nk_BT}{2} tr(\boldsymbol{\mu} - \mathbf{I}) + p(det(\mathbf{F}) - 1) \quad \text{and} \quad \mathcal{D} = k_d\Psi \tag{5}$$

where p is the hydrostatic pressure that enforces incompressibility. The expression for $\mathcal{D}$ shows that the detachment of chains at their stress state leads to unrecoverable loss of elastic stored energy at rate k_d. Since Eqs. (2) and (4) are formulated in an incremental form, the variables $\boldsymbol{\mu}$, Ψ and $\mathcal{D}$ already contain the information about deformation history and therefore convolution integral is not needed. Finally, the Cauchy stress tensor $\boldsymbol{\sigma}$ is finally given by Vernerey and Long (2017):

$$\boldsymbol{\sigma} = nk_BT(\boldsymbol{\mu} - \mathbf{I}) + p\mathbf{I} \tag{6}$$

2.2. Competition between chain stretch and dynamics

Eq. (4) shows that the chain conformation tensor $\boldsymbol{\mu}$ results from a kinetic competition between the rate of network deformation and bond dynamics. This competition is usually quantified by the Weissenberg number:

$$W = \frac{\dot{\epsilon}}{k_d} \tag{7}$$

where $\dot{\epsilon}$ is the true strain rate. To illustrate this, let us consider the pure shear extension of a specimen (Fig. 2a) whose geometry is defined by its width L_0, height H_0 and thickness b_0 with $L_0 \gg H_0 \gg b_0$. Due to these geometrical constraints, the horizontal deformation is negligible and the deformation gradient at any time t is $\mathbf{F} = diag\{1,\ \lambda,\ 1/\lambda\}$ with $\lambda(t) = exp(\dot{\epsilon}t)$ while the velocity gradient thus is $\mathbf{L} = diag\{0,\ \dot{\epsilon},\ -\dot{\epsilon}\}$. During deformation, the evolution of chain conformation can be determined from Eq. (4) as:

$$\begin{aligned}
\dot{\mu}_{11} &= k_d\left(\frac{3}{\mu_{11}^{-1} + \mu_{22}^{-1} + \mu_{33}^{-1}} - \mu_{11}\right)\\
\dot{\mu}_{22} &= k_d\left(2W\mu_{22} + \frac{3}{\mu_{11}^{-1} + \mu_{22}^{-1} + \mu_{33}^{-1}} - \mu_{22}\right)\\
\dot{\mu}_{33} &= k_d\left(-2W\mu_{33} + \frac{3}{\mu_{11}^{-1} + \mu_{22}^{-1} + \mu_{33}^{-1}} - \mu_{33}\right)
\end{aligned} \tag{8}$$

The rate of change of elastic stored energy is therefore computed from Eq. (5) as:

$$\dot{\Psi} = \frac{nk_BT}{2}[2Wk_d(\mu_{22} - \mu_{33}) - k_d(2 - \mu_{22} - \mu_{33})]. \tag{9}$$

The first term on the right-hand side quantifies the rate of energy density gained from external work ($\dot{\mathcal{W}}$) since $\dot{\mathcal{W}} = \boldsymbol{\sigma} : \mathbf{L} = nk_BTWk_d(\mu_{22} - \mu_{33})$ while the second term $k_d\frac{nk_BT}{2}[(\mu_{22} + \mu_{33} - 2)] = k_d\Psi = \mathcal{D}$ accounts for the rate of energy dissipation due to bond dynamics. Fig. 2b plots $\dot{\Psi}$ as a function of chain stretch λ for different values of W. Our results show that the system can be found into two regimes:

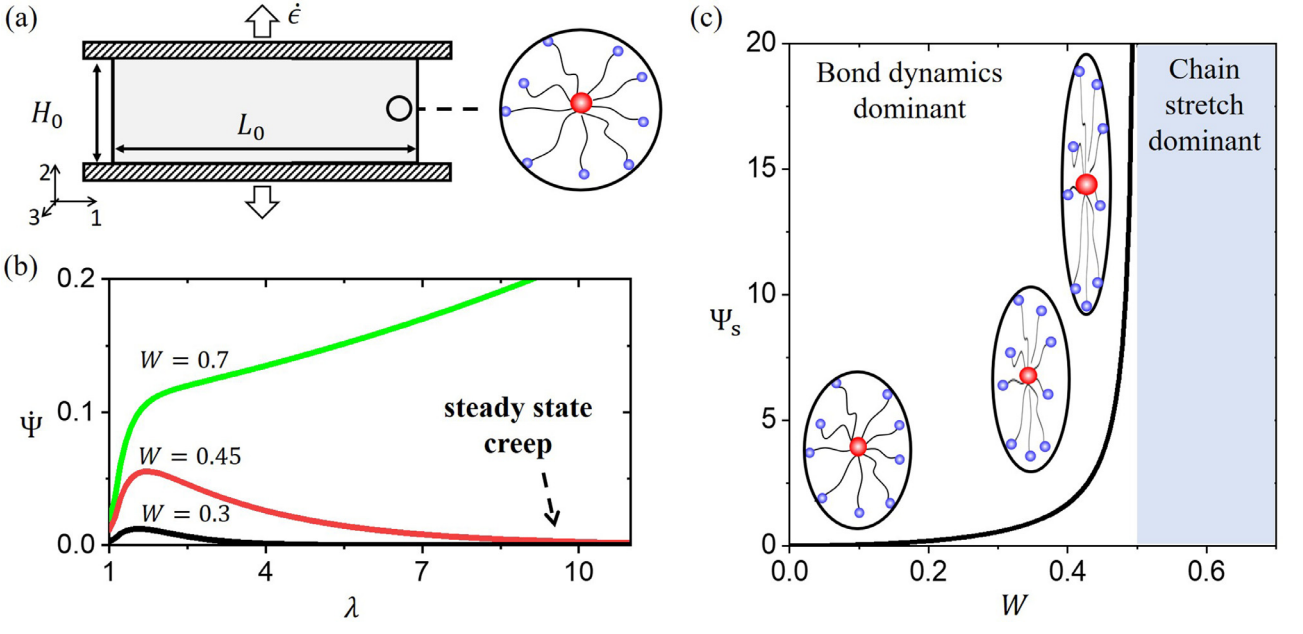

Fig. 2. (a) Schematic of pure shear tensile experiment. The specimen's dimension is $L_0 \gg H_0$. (b) The rate of change in stored elastic energy density $\dot{\Psi}$ as a function of stretch H/H_0 at different rates. (c) The stored elastic energy density at the steady state Ψ_s as a function of Weissenberg number W.

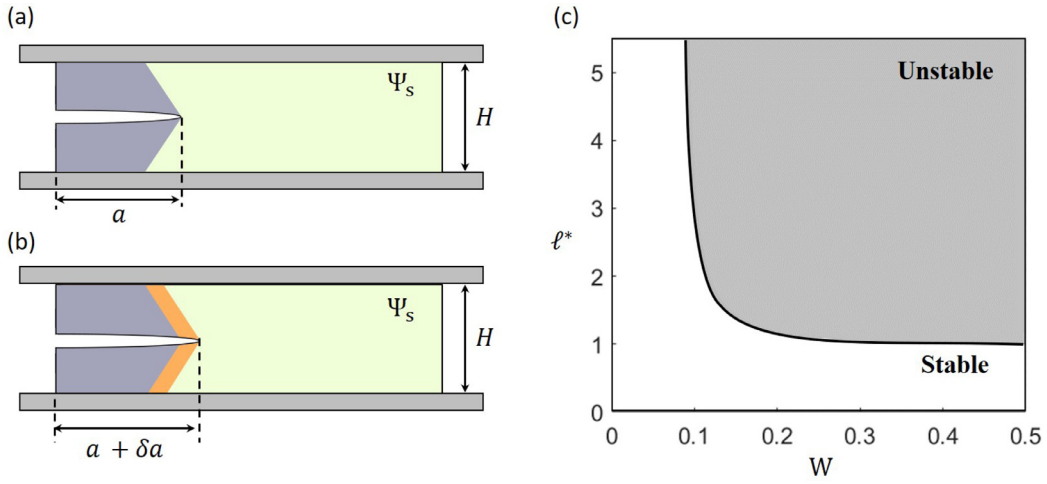

Fig. 3. Schematic of a pure shear sample (a) before and (b) after the crack propagates by a small increment δa. (c) A phase diagram that shows the stable and unstable regime for the case when the specimen's stretch is fixed after the crack propagates.

a. When $W < 0.5$, the rate of change of stored elastic energy density always asymptotes to zero in the long term. The condition $\dot{\Psi} = 0$ characterizes steady-state creep condition where the external work is balanced with viscous dissipation. As a result, the chain conformation remains unchanged although λ continuously increases. The steady state values of $\boldsymbol{\mu}$ can therefore be obtained by considering $\dot{\mu}_{22} = 0$ and $\dot{\mu}_{33} = 0$ in Eq. (8). Further using Eq. (5), the steady state stored elastic energy Ψ_s at steady state is found as Lalitha Sridhar and Vernerey (2018):

$$\Psi_s = \frac{E}{6}\left[\frac{3 - 4W^2}{(1 - 4W^2)^{2/3}} - 3\right] \tag{10}$$

This $\Psi_s - W$ relation is plotted in Fig. 2c along with schematics of chain conformations, where we see that Ψ_s diverges as W approaches 0.5, indicating that chain elastic stretch becomes predominant.

b. When $W \geq 0.5$, the stored elastic energy increases monotonically with time. In this case, the rate of network deformation is too large to be compensated by bond dynamics and a steady state cannot be obtained.

2.3. Crack stability in transient networks: case study

When a crack nucleates in a transient network, its stability depends on the interplay between four energetic quantities: the incremental work $\delta\mathcal{W}$ done by external loading per unit area of crack, the elastic energy release rate G_e, the work G_0 required to create a unit area of crack surface and the viscous dissipation G_v per unit crack extension. Crack propagation is energetically favored if Zehnder (2012):

$$\delta\mathcal{W} + G_e \geq G_0 + G_v. \tag{11}$$

Physically, this equation states that the energy available for crack advance needs to be greater than the energy being dissipated (by both viscoelasticity and crack advance). For the case of an elastic material ($G_v = 0$), it has been shown in experiment that the crack propagates at steady state when external deformation is kept at a fixed level ($\delta\mathcal{W} = 0$) (Qi et al., 2019). In this case, the fracture criterion (eq. (11)) degenerates to $G_e \geq G_0$, a condition that has been widely applied for steady state elastic fracture (Zehnder, 2012). For the case of a pure shear fracture test (Fig. 2a), the stability of an elastic crack is typically explored by first subjecting the sample of height H_0 to a fixed level of stretch. If Ψ_f is the stored elastic energy at the far field, it can be shown that the crack becomes unstable and propagates when $\Psi_f H_0 \geq G_0$. In this regime, the crack propagates at steady-state with constant velocity (Long and Hui, 2016).

In the case of transient networks, this approach must be revisited since the elastic energy Ψ_f does not only depend on stretch, but is also a function of the rate of loading (Fig. 2b & c). To examine this situation, consider a pure shear specimen in steady-state creep conditions ($W < 0.5$), that is suddenly cut with an edge crack of length a (Fig. 3a). To simplify the analysis, we further make four assumptions: (a) the loading ceases as soon as the crack is introduced (i.e. $\delta\mathcal{W} = 0$ in the post-crack regime). (b) the deformation is small enough so that the crack does not blunt as it propagates and $H \approx H_0$. (c) the crack velocity v is constant and independent of loading condition. (d) Finally, similar to the Griffith theorem (Zehnder, 2012), the elastic energy Ψ_s is assumed to be uniform in the material ahead of the tip (the green region in Fig. 3a). We note that these assumptions will be relaxed in the next section, so that general cases can be considered. In this case, the crack stability criterion (Eq. (11)) becomes $G_e - G_v \geq G_0$. The elastic energy release rate is calculated as $G_e = \delta\Pi_e/\delta a$ where $\delta\Pi_e = \Psi H_0 \delta a$ quantifies the elastic energy loss per area due to the addition of unloaded material (shown by the yellow region in Fig. 3b).

The viscous viscous dissipation is calculated as $G_v = \delta\Pi_v/\delta_a$ where $\delta\Pi_v = k_d\Psi A\delta t$ represents the loss of elastic energy in the bulk due to bond dynamics (green region of area A in Fig. 3a) over time interval $\delta t = \delta a/v$. Recalling that $L >> H$ for pure shear geometry, the area of the green region can be calculated as $A = H(L-a) + \mathcal{O}(H^2)$. Neglecting the higher order term, G_e and G_v are evaluated as:

$$G_e = \Psi_s H_0 \quad \text{and} \quad G_v = \frac{k_d}{v}\Psi_s H_0 (L-a) \tag{12}$$

and the crack stability criterion becomes

$$\Psi_s H\left[1 - \frac{1}{\ell}(L-a)\right] \geq G_0 \tag{13}$$

where $\ell = v/k_d$ is a characteristic length that characterizes the competition between crack propagation and viscous dissipation. According to De Gennes (1996), this length represents a region around the crack tip within which crack propagates in a quasi-elastic manner. Interestingly, when the ratio $\ell^* = \ell/(L-a) \gg 1$, Eq. (13) degenerates to the criterion for elastic materials because the crack propagates fast enough so that the bulk dissipation becomes negligible. The criterion of Eq. (13) can be visualized in a phase diagram for crack stability as a function of W and ℓ^* (Fig. 3c)where we see that bulk dissipation affects the crack stability in two ways. During the loading stage, it competes with external loading (measured by W) that determines the stored elastic energy density Ψ_s in the far field. After the cut is introduced, the bulk dissipation also competes with the energy loss due to crack propagation. Eventually, we find that crack propagation is only favorable when $\ell^* > 1$, i.e., the full specimen behaves elastically during the event of fracture (De Gennes, 1996; Saulnier et al., 2004). When $\ell^* < 1$, bulk dissipation plays a predominant role and the crack is stable regardless of W; this is contrary to elastic fracture where crack stability is directly related to a critical value of Ψ_s. This finding explains the enhanced flaw tolerance of viscoelastic materials in adhesion applications (Creton and Ciccotti, 2016) as the viscosity not only decreases the energy in the bulk during the loading stage, but also shields the crack from propagation. Since fracture becomes less likely to occur, bulk deformation (e.g., cavitation, fingers pattern formation) becomes a common mode of failure in applications.

This result also indicates that in a viscoelastic fracture experiment, the protocol of fixing deformation during crack propagation becomes inappropriate because bulk dissipation may prohibit the crack from propagating. To address this, we recall from Fig. 2b that the contribution of bulk dissipation can be balanced out by external work if the specimen is continuously stretched with constant W. In this case, the crack stability criterion becomes $\Psi_s H \geq G_0$ which only depends on W. Furthermore, in analogy to the critical stretch ratio for elastic materials, the crack stability criterion can be converted into a critical loading rate W which can be easily measured. However, we emphasize that this analysis is based on the assumption of small deformation and uniform stress fields and the crack is introduced in a steady state creep condition. In practice, the crack is usually introduced before the specimen is stretched and the stretch level is usually more than 30% (Ghatak et al., 2000; Liu et al., 2019b; Luo et al., 2014), beyond which the material behaves nonlinearly. In addition, the fracture process is also more complicated, wherein the crack velocity is not an intrinsic material property but a function of crack driving force (Ghatak et al., 2000). It also does not necessarily take on an (elastic) parabolic profile since blunting may occur during propagation (De Gennes, 1996; Saulnier et al., 2004). Gaining a comprehensive understanding of the above features requires a framework that incorporates nonlinear viscoelasticity and an accurate description of the stress fields, where an analytical solution is difficult to obtain. As an alternative, we develop here a numerical framework that is based on our previous work (Shen et al., 2019b) to capture and unveil the mechanisms behind experimental observations.

3. A general framework for viscoelastic fracture

In this section, we introduce a general framework for viscoelastic fracture of transient networks at finite strain. This framework is introduced on the basis of a finite element computational model developed previously that can accurately describe the combined flow and elastic deformation in viscoelastic solids at large deformation. Notably, this computational model is developed based on the Eulerian description of kinematics and therefore it can handle the arbitrary deformation levels of material without losing accuracy. Readers are referred to Appendix C for details on the solution strategy and Foucard et al. (2015); Shen et al. (2019b) on the numerical scheme. In this section, using the stress field solution from the finite element simulations, we focus on the crack stability criterion (Eq. (11)) and the relationship between rate-dependent chain rupture and crack velocity.

3.1. General framework for crack stability in transient networks

To evaluate the fracture criterion (Eq. (11)), let us consider the extension of a cut specimen of height H as shown in Fig. 6a. During a small time increment δt, this specimen evolves to state b shown in Fig. 4b, where the crack extends by δa with velocity v. The quantities $\delta\mathcal{W}$, G_e and G_v are evaluated between these two states. For this, the first step is to numerically solve for the stress fields, stored elastic energy and the work of external load $\delta\mathcal{W}$ per unit crack length can be computed as:

$$\delta\mathcal{W} = \frac{1}{b\delta a}\int_0^{\delta t}\int_V \boldsymbol{\sigma} : \mathbf{L}\, dV dt. \tag{14}$$

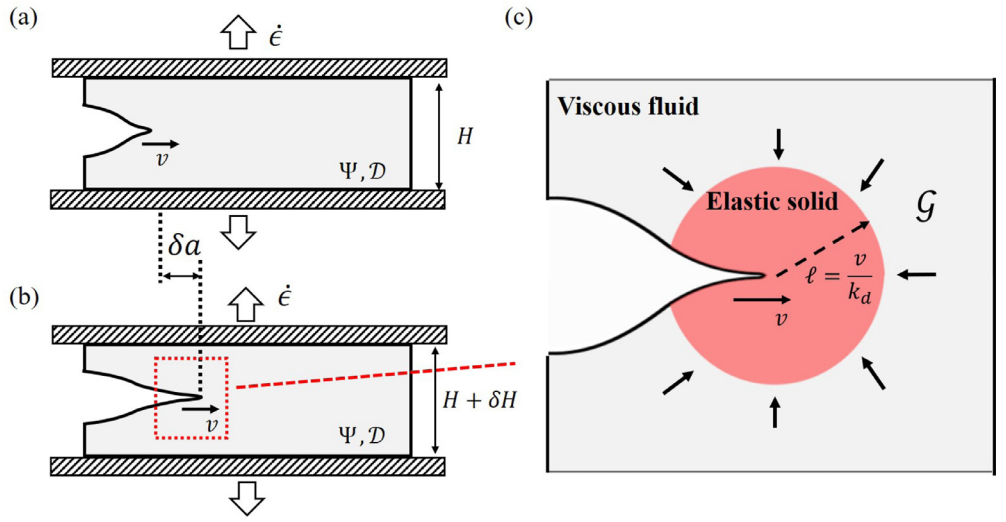

Fig. 4. The crack tip driving force is calculated based on the evolution from state (a) to (b) over a period of time δt. (c) Schematic of different regimes around the crack tip based on the role of bulk dissipation. The crack tip driving force $\mathcal{G}$ can be interpreted as the energy flow to the elastic solid regime.

where b is the specimen's thickness and $\int_V^* dV$ denotes the integration over the specimen's volume. We note that the divergence theorem was used in Eq. (14) in order to relate the traction on the boundary to the stress in the bulk. The elastic energy release rate G_e is by first computing the change of elastic stored energy at each material point $\delta\Psi$ between state a and b, and then integrating over the specimen's volume as:

$$G_e = \frac{1}{b\delta a}\int_V \delta\Psi dV. \tag{15}$$

Finally, the viscous dissipation G_v is computed by integrating the rate of dissipation from state (a) to (b) as:

$$G_v = \frac{1}{b\delta a}\int_0^{\delta t}\int_V \mathcal{D} dV dt. \tag{16}$$

We note that since $\delta t = \delta a/v$ and $\mathcal{D} = k_d\Psi$, the above equation implies a scaling of $G_v \propto 1/\ell$, where we again see the appearance of the trumpet length $\ell = v/k_d$. According to De Gennes (1996), dissipative term is responsible for different crack profiles between the vicinity of the crack and the far field, yielding a "trumpet" profile schematically depicted in Fig. 4c. This argument has been confirmed by several experimental studies (Saulnier et al., 2004; Sun et al., 2017; Tabuteau et al., 2011) based on the crack tip profile. One can finally define the crack driving force $\mathcal{G}$ as:

$$\mathcal{G} = \delta\mathcal{W} + G_e - G_v. \tag{17}$$

The crack stability criterion is therefore expressed as the difference between the crack driving force $\mathcal{G}$ and the intrinsic fracture toughness G_0, i.e., the crack is unstable if $\mathcal{G} \geq G_0$ (as provided by Eq. (11)). The variable $\mathcal{G}$ can be interpreted as the energy flow to the elastic domain near the crack tip (Fig. 4c). To fully capture the fracture process, two quantities however remain to be determined: the crack velocity v and the intrinsic fracture toughness G_0. Both quantities are associated with rupture of dynamic bonds occurring at the crack tip, whose characteristic length scale is beyond the resolution of continuum framework. This is discussed in the following section.

3.2. Kinetics of chain rupture and crack propagation

At the molecular scale, the crack tip advances by progressively breaking the chains that bridge the interface. A conventional model to describe this process is the Lake-Thomas (LK) theory (Lake and Thomas, 1967) that considers each chain as an elastic spring that only ruptures at a critical stretch. In this case, the fracture toughness is only related to the level of deformation and considered rate-independent. This situation is however not applicable to the case of transient networks because the concept of "rupture length" cannot be defined. Due to the transient nature of the mechanical bonds, a chain can indeed break at any state. An alternative consideration was first proposed by Chaudhury (1999) where fracture is caused by the accelerated bond dissociation at the tip due to the fact that k_d increases with force (Eq. (1)). Based on this physical picture, Chaudhury (1999); Ghatak et al. (2000) and Hui et al. (2004) have thoroughly formulated the problem of chain damage at the crack tip and have established a crack driving force ($\mathcal{G}$)-velocity (v) relationship. In what follows, the relationship and the intrinsic fracture energy G_0 are determined based on their works.

Let us first take a close look at the tip of a traveling crack shown in Fig. 5a, where the chains bridging the interface, with aerial density $\tilde{n}$, are stretched progressively. According to Lake and Thomas (1967), for a uniform network, $\tilde{n} = \frac{1}{2}\xi_0 n$

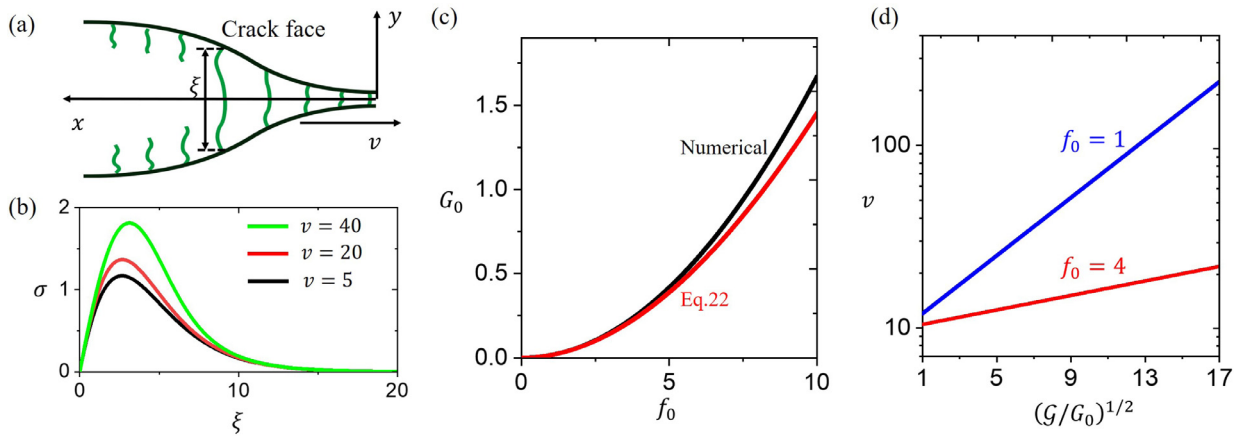

Fig. 5. (a) Schematic of the progressive chain stretch at the tip as the crack propagates. (b) An example for the stress (σ)- separation (ξ) relation for three different crack velocities obtained by numerically solving Eq. (18). (c) The comparison between numerical solution of intrinsic fracture toughness G_0 from Eq. (21) and the analytical approximation using Eq. (22). (d) Examples of crack velocity as a function of crack tip driving force $\mathcal{G}$ given by Eq. (23).

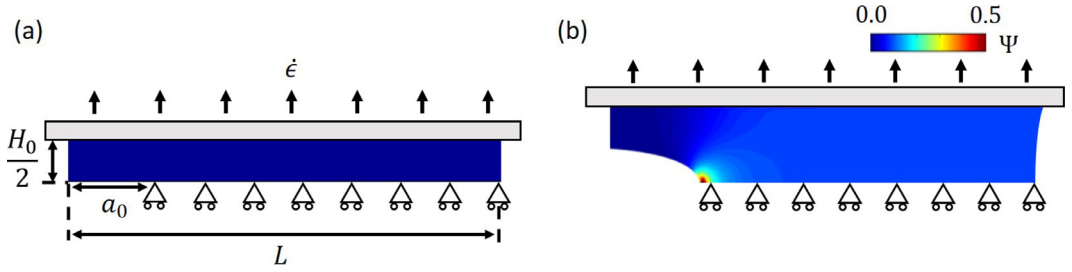

Fig. 6. An example of the finite element simulation and boundary condition. (a) the undeformed state and (b) deformed state of the specimen.

where $\xi_0 = \sqrt{N}b$ is the average chain length at the stress-free configuration with N the Kuhn number and b the Kuhn length (Lake and Thomas, 1967). At the continuum level, the chain dynamics k_a and k_d are assumed to be constant because the stress level is usually relatively low compared to the tip. However, this assumption fails to hold at the tip, where stress is highly concentrated and k_a and k_d are typically force-sensitive, as described by the Eyring's theory (Eq. (1)). Consequently, chains at the tip experience two concurring processes: localized stretch caused by crack opening and damage due to accelerated dissociation. Considering a local coordinate whose origin moves together with the crack tip (Fig. 5a), the change in chain density along the x coordinate satisfies the convection equation $v\partial\bar{n}/\partial x = d\bar{n}/dt$. Using Eq. (2), this equation can further be rewritten as :

$$v\alpha\frac{\partial\bar{n}}{\partial\xi} = k_a(\bar{n}_t - \bar{n}) - k_d\bar{n} \tag{18}$$

where we applied the chain rule $v\partial\bar{n}/\partial x = d\bar{n}/dt$ and $\alpha = \partial\xi/\partial x$ is a parameter that characterizes the crack profile. An accurate solution of this quantity is not yet available since it requires a multi-scale analysis that couples chain damage at the crack tip to the deformation of the bulk material. Since this is not the focus of this work, we here follow the approximation of Chaudhury (1999) and Ghatak et al. (2000) and idealize the crack profile as a wedge with slope $\alpha = 1$. The above equation leads to a $\bar{n} - \xi$ relationship for the chains bridging the crack. Further considering linear chains with stiffness k, a stress ($\sigma = \bar{n}k\xi$) - separation (ξ) relation is then obtained, as plotted in Fig. 5b for different values of crack speed v. The crack driving force $\mathcal{G}$ is computed by the work done to break bridging chains per unit area of crack surface, which equals to the area under the $\sigma - \xi$ curve:

$$\mathcal{G} = \int_0^\infty \sigma\, d\xi. \tag{19}$$

Generally, there is another contribution to $\mathcal{G}$ due to network damage (i.e., nonlocal chain rupture, void nucleation and growth) within a region of length ξ_d around the crack tip (Long et al., 2020). For ductile materials, ξ_d is large (~ mm) and the crack tip damage becomes the major contribution to $\mathcal{G}$. For brittle materials, which is the focus of this work, ξ_d is comparable to chain length and crack tip damage is negligible (Long et al., 2020). As a result, Eq. (19) only describes the energy consumed by the rupture of bridging chains. Although an analytical solution for Eqs. (18) and (19) is not available, Chaudhury (1999) obtained a closed-form approximation by determining the average length for bond rupture $\bar{\xi}$. This was done under two assumptions: **(i)** *the bond association rate k_a is negligible compared to the dissociation rate k_d;* **(ii)***the mag-*

nitude of crack velocity satisfies $v/k_d^0 \gg f_0/k$. In these conditions, the $v-\mathcal{G}$ relation was obtained as (detailed derivations in Appendix B):

$$v = \frac{f_0 k_d^0}{k} \exp\left(\frac{1}{f_0}\sqrt{\frac{2k\mathcal{G}}{\bar{n}}}\right) \tag{20}$$

The two assumptions made by Chaudhury are justified as follows. First, chains are highly stretched as the crack interface opens. Since k_d increases exponentially with force and k_a decreases exponentially, $k_a \ll k_d$ is satisfied (Fig. 1b). Second, the trumpet length ($\ell = v/k_d^0$) is a macroscopic quantity while the term f_0/k scales with the length of a chain. Therefore, the assumption $v/k_d^0 \gg f_0/k$ is valid as long as crack propagation is macroscopically observable. In experiment, this $ln(v) - \sqrt{\mathcal{G}}$ relationship has been reported in several studies (Chaudhury, 1999; Ghatak et al., 2000).

By contrast, the intrinsic fracture toughness G_0 was not determined in the work of Chaudhury. This quantity can be defined as the energetic threshold for interface breakage and represents the energy required to break the chains via a chemical equilibrium process ($d\bar{n}/dt = 0$) (Lavoie et al., 2016). In this scenario, the concentration of connected chains is only a function of stretch through k_a and k_d as $\bar{n} = \bar{n}_t k_a/(k_a + k_d)$. Plugging this relation into (19), G_0 is calculated by the following integral:

$$G_0 = \bar{n}_t k \int_0^\infty \frac{\xi}{1 + \frac{k_d^0}{k_a^0} exp\left(\frac{2k}{f_0}\xi\right)} d\xi. \tag{21}$$

While this integral is difficult to evaluate analytically, a closed-form can be obtained by approximating the integrand with an isosceles triangle as (details shown in Appendix B):

$$G_0 = \left(\frac{\bar{n}_t f_0^2}{k}\right) \frac{\mathcal{A}^2}{2[1 + \exp(\mathcal{A})]} \tag{22}$$

Here $\mathcal{A} = W_0(\frac{k_a^0}{k_d^0}\frac{1}{e}) + 1$ with $W_0(^*)$ the main branch of Lambert W function (Lambert, 1758). Fig. 5c compares the numerical calculation (via Eq. (21)) and analytical approximation (Eq. (22)) the of $G_0 - f_0$ relationship, where we see that a reasonable match is obtained. In addition, we confirm that G_0 is an intrinsic material property that only depends on chain concentration $\bar{n}_t$ and the force sensitivity f_0 of the bond. If the bonds are less sensitive to force (larger f_0), G_0 increases since the accelerated chain damage occurs at a higher stretch level. In summary, the stability and velocity of a crack follows the rule:

$$v = \begin{cases} 0, & \mathcal{G} < G_0 \\ \dfrac{f_0 k_d^0}{k} \exp\left(\dfrac{1}{f_0}\sqrt{\dfrac{2k\mathcal{G}}{\bar{n}}}\right), & \mathcal{G} \geq G_0 \end{cases} \tag{23}$$

The above rule suggests a minimum crack velocity v_0 at $\mathcal{G} = G_0$, which can be regarded as the characteristic fracture velocity that solely depends on the intrinsic material properties f_0 and $\bar{n}_t$.

4. Dynamic regimes in pure shear fracture tests

Using our general framework, we here study the various dynamic regimes one may encounter during the pure shear fracture test of transient networks. For this, we focus on two parameters that control the rate-dependent fracture: (a) the Weissenberg number $W = \dot{\epsilon}/k_d^0$ that measures the competition between external load and bulk dissipation and (b) the normalized Trumpet length $\ell^* = \ell/(L - a_0)$ that describes the interplay between crack propagation and bulk dissipation. In what follows, all numerical simulations are performed using a customized program written in Matlab. Fig. 6 shows an example of numerical simulation, where only the top half of a shear crack sample is included due to the symmetry of the problem (Fig. 6a). The bottom boundary at the bottom is divided into two parts, the traction free crack surface of length a_0 and a "solid" section whose vertical motion is constrained. When the crack is unstable, these constraints are removed sequentially to create new crack surfaces. To avoid boundary effects at the right edge, we consider a wide specimen whose width L, initial height H_0 and initial crack length a_0 follow $H_0 = L/15$ and $a_0 = L/12$. In our study, we choose a network with intrinsic fracture toughness $G_0 = \bar{n}_t f_0^2/3k$ which, according to Eq. (22), characterizes a material with $k_a^0 = k_d^0$.

4.1. Characteristic fracture behaviors

We perform our study by considering three loading rates measured by $W = 0.07,\ 0.3$ and 0.7. For each loading rate, we investigate the behavior of a slow crack ($\ell^* = 0.2$) and a fast crack ($\ell^* = 1.3$), respectively. In all cases, we explore the change in crack velocity v and crack profile over time, and track the evolution of the crack driving force $\mathcal{G}$.

Slow loading ($W = 0.07$). In the case where the specimen is loaded slowly ($W = 0.07$), our results show that the crack remains stable regardless of ℓ^*. Fig. 7a exhibits three simulation snapshots, where the contour plots the stored elastic energy

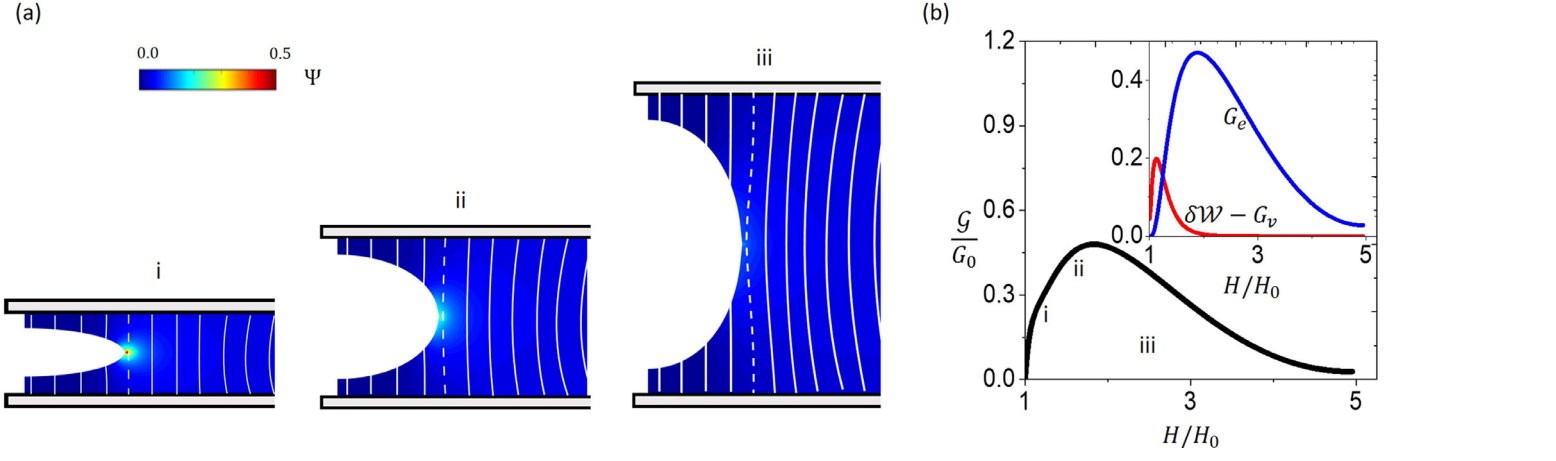

Fig. 7. (a) Three snapshots for the crack blunting for $W = 0.07$ and $\ell^* = 1.3$. (b) Evolution of crack tip driving force $\mathcal{G}$ as a function of stretch H/H_0. The subfigure shows the evolution of $\delta\mathcal{W} - G_v$ and G_e. Both quantities are normalized by G_0.

density Ψ in the network, of a specimen with $\ell^* = 1.3$. Vertical stripes are plotted on the specimen to visualize deformation and track the crack position. To understand the energy flow in the material, Fig. 7b further plots the change of $\mathcal{G}$ as a function of stretch H/H_0 and the inset shows the contribution of each mechanism that are represented in Eq. (17). In this scenario, since viscous dissipation is predominant, the specimen reaches steady state creep as $\delta\mathcal{W} - G_v \to 0$ and the level of stored elastic energy density in the far field remains low (Fig. 7a). As a result, the crack driving force $\mathcal{G}$ is insufficient to propagate the crack (Fig. 7b). Interestingly, our results show that further stretching the specimen leads to a decrease in $\mathcal{G}$. This is because the increase in stretch leads to crack blunting and a decrease in stress concentration, as exhibited by the snapshots of Fig. 7a. Eventually, the crack does not propagate for any level of stretch. This phenomenon has been observed in the extensional fracture test of associative polymers. For instance, in the uniaxial extensional flow experiment of a PRMO-Na ionomer filament (Shabbir et al., 2016), the filament thins continuously without breaking as $W \to 0$.

Fast loading ($W > 0.1$), fast crack ($\ell^* = 1.3$)**.** As we maintain $\ell^* = 1.3$ and increase W continuously, we observe that the crack becomes unstable and propagates in a steady state. Steady state propagation is characterized by a fast crack that travels at constant velocity through the specimen at nearly constant external stretch H/H_0. Fig. 8a exhibits two examples for $W = 0.3$ and 0.7, respectively, where we clearly see the effect of W from the crack profile. For $W = 0.7$, elastic stretch is predominant ahead of the crack and the unloaded chains retract to their undeformed state in the wake of the crack, leading to a parabolic profile reminiscent of elastic fracture. For $W = 0.3$, bulk dissipation becomes non-negligible, which leads to two notable observations. First, fracture occurs at a much larger stretch than when $W = 0.7$ (Fig. 8a) because a larger portion of energy is consumed by bulk dissipation. Second, the chains behind the crack tip are unloaded to a deformed state, making the crack surface deviate from its original parabolic profile. In this case, the crack surface is characterized by two parabolic shapes, a blunt one that belongs to the region of the initial cut and a sharp one for the new surface created by the propagating crack. In experiment, this crack profile has recently been observed in the fracture of a dual crosslinked hydrogel, where the initial cut blunts during loading and a sharp "secondary" crack is initiated at the tip of the blunt region (Liu et al., 2019b). During propagation, the crack travels at a constant velocity for both values of W (Fig. 8b) and exhibit a self-similar profile over time (Fig. 8c). Taking together, these results imply steady state crack propagation since both the far field stress and deformation remain invariant with respect to the tip during propagation (Long and Hui, 2016). We find that this condition is satisfied when the crack speed is very fast ($\ell^* > 1$) compared to the rates of bond dynamics and external load.

Furthermore, steady state propagation is examined when the crack tip driving force $\mathcal{G}$ is equal to the intrinsic fracture energy G_0. For an elastic solid in pure shear condition, $\mathcal{G}$ is computed as Long and Hui (2016):

$$\mathcal{G} = H_s \Psi_f. \tag{24}$$

where H_s is the height of the specimen at the stress free state, which equals the undeformed height for the elastic specimen. The quantity Ψ_f is the stored elastic energy density at the far field, which can also be determined from an uncut sample, with identical geometry, that experiences the same loading history. However, this equation cannot be directly applied to viscoelastic material at finite strain since the solid deforms permanently due to creep. As a result, H_s is not equal to the undeformed height and cannot be directly measured. To address this, previous work of Mayumi et al. (2016) suggests that H_s can be obtained from the uncut sample. At the onset of crack propagation, H_s can be determined by rapidly unloading the uncut sample to its stress-free state. While this can be done experimentally, the transient network theory provides a convenient way to calculate H_s through the conformation tensor $\boldsymbol{\mu}$ which directly measures the mean squared stretch of chains. First, for pure shear geometry, $\boldsymbol{\mu}$ can be determined by solving Eq. (8) through the loading history. H_s is then related to the vertical component μ_{22} at propagation as $H_s = H/\sqrt{\mu_{22}}$ where μ_{22} can be determined from Eq. (8) (derivation provided in Appendix D). The crack driving force is then calculated as:

$$\mathcal{G} = \frac{H}{\sqrt{\mu_{22}}} \Psi_f. \tag{25}$$

To check the accuracy of Eq. (25), we compare its prediction with simulation results for different values of W (Fig. 8d) where we keep $\ell^* = 1.3$ to ensure steady propagation. A good agreement is achieved for different values of W, validating the applicability of Eq. (25) for steady state propagation.

Fast loading ($W > 0.1$), slow crack ($\ell^* = 0.2$)**.** When the crack velocity becomes slower, the role of external load and bulk dissipation becomes more pronounced. Thus, when the specimen is loaded at $W = 0.3$, we observe a peculiar behavior in which the crack first propagates but eventually stops and blunts (Fig. 9a). We further see from Fig. 9b that the crack first accelerates then starts decelerating monotonically to a zero speed. This is accompanied by a sharpening-blunting evolution of the crack profile depicted in the inset of Fig. 9b. To explain this process, Fig. 9c plots the evolution of energy flow as functions of H/H_0, where we see that in this case, the crack driving force $\mathcal{G}$ first increases as $\delta\mathcal{W} - G_v > 0$, triggering crack initiation. However, recalling that at the far field, viscous dissipation gradually reaches the steady state creep condition as $W < 0.5$ (Fig. 2b), further stretching the specimen does not provide more energy to the crack for propagation. This occurs in Fig. 9c as $\delta\mathcal{W} - G_v$ gradually decreases to zero. Instead, it causes crack blunting and a decrease in stress concentration. As a result, the magnitude of G_e decreases upon further stretching and $\mathcal{G}$ eventually becomes smaller than G_0, at which time the crack is arrested.

When W is further increased to 0.7, we find that the crack propagates in an accelerated manner as shown in Fig. 10a. As it accelerates with elongation H/H_0, the crack tip sharpens (inset of Fig. 10b) which subsequently leads to a higher level of

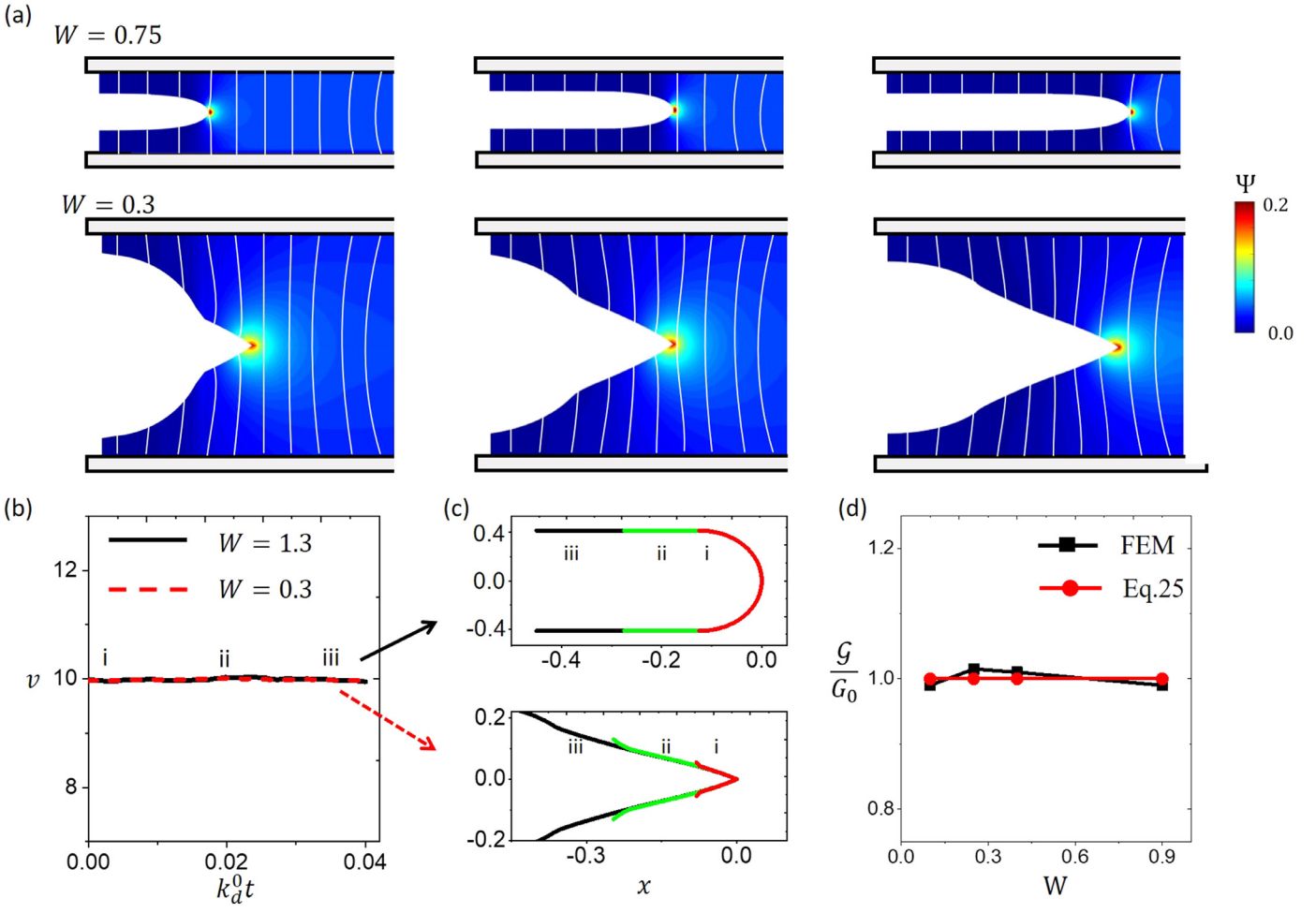

Fig. 8. (a) Four snaps of the crack propagation in the specimen for a fast crack $\ell^* = 1.3$ with loading rates $W = 0.75$ and $W = 0.3$, respectively. (b) Evolution of crack velocity during the propagation. (c) The overlap of crack tip profiles when they are moved to a common tip. (d) Comparison of the crack tip driving force $\mathcal{G}$ computed by finite element framework and by Eq. 25.

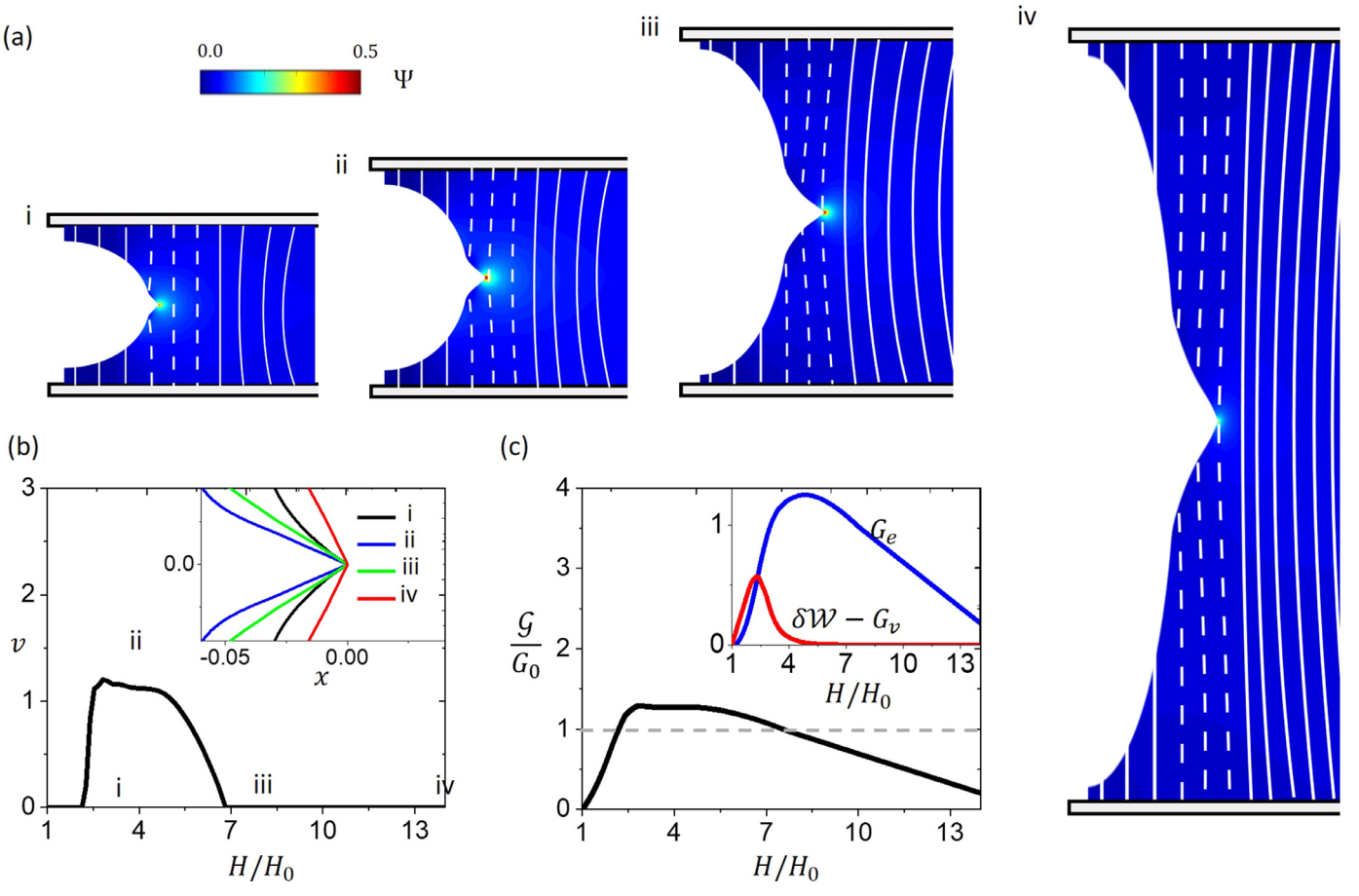

Fig. 9. (a) Four snaps for the crack propagation in the specimen for $\ell = 0.2$ and $W = 0.3$. Three vertical lines are marked with symbols on the top plate to help visualize crack propagation. (b) Change of crack velocity v as a function of stretch H/H_0. The subfigure shows the crack tip profile of each snapshot in (a) at a common coordinate. (c) Evolution of crack tip driving force $\mathcal{G}$ as a function of stretch H/H_0. The subfigure shows the evolution $\delta\mathcal{W} - G_v$ and G_e. Both quantities are normalized by G_0.

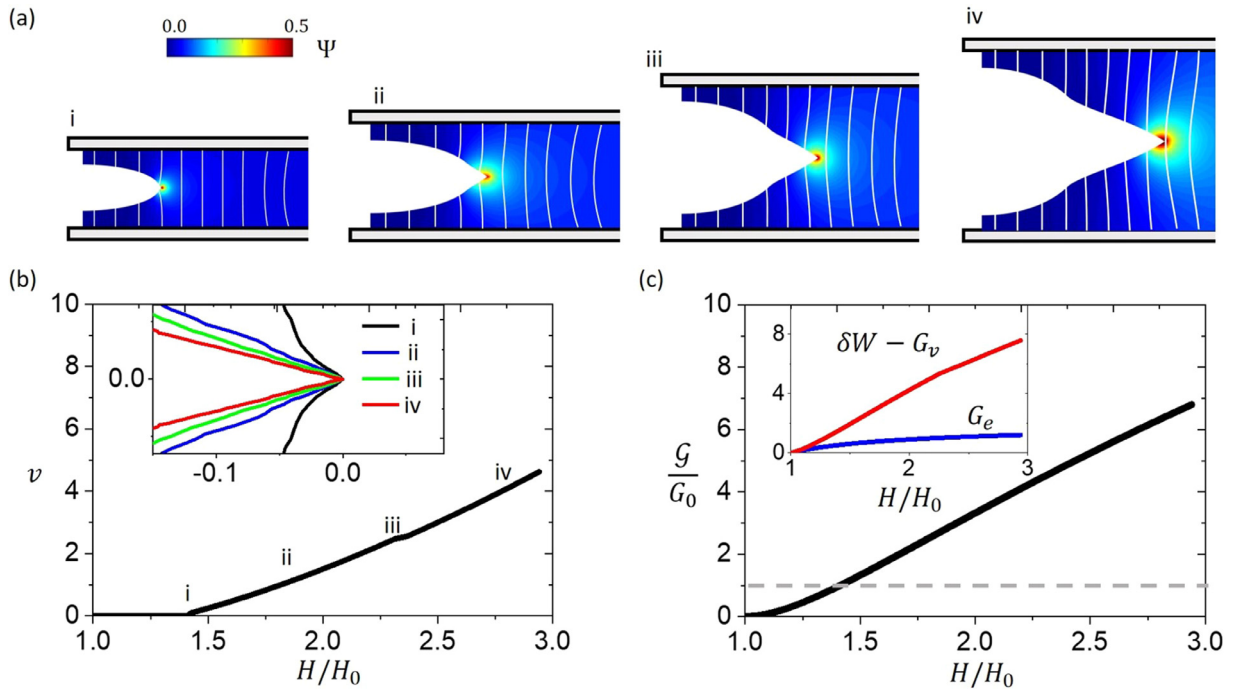

Fig. 10. (a) Four snapshots of the crack propagation in the specimen for $\ell^* = 0.2$ and $W = 0.7$. (b) Change of crack velocity v as a function of stretch H/H_0. The subfigure shows the crack tip profile of each snapshot in (a) at a common coordinate. (c) Evolution of crack tip driving force $\mathcal{G}$ as a function of stretch H/H_0. The subfigure shows the evolution $\delta\mathcal{W} - G_v$ and G_e. Both quantities are normalized by G_0.

stress concentration (Long and Hui, 2015), as shown by the contour plot in Fig. 10a. To understand the mechanism behind this observation, we plot in Fig. 10c the evolution of $\mathcal{G}$ as a function of H/H_0 and the detailed contribution of each term in Eq. (17). Since $W > 0.5$, external work is predominant over the bulk dissipation (as shown by the increasing $\delta\mathcal{W} - G_v$) which causes a monotonic increase in the stored elastic energy and G_e. The above mechanisms collectively increase the crack tip driving force $\mathcal{G}$ and result in an accelerating crack. Based on this analysis, we postulate that an accelerating crack is always expected when $W > 0.5$ since the external work keeps feeding an excess amount of energy to the material.

4.2. A phase diagram for rate-dependent fracture

To summarize the various dynamic behaviors of a crack in a transient network, we performed a parametric study for range $W \in [0.06, 0.8]$ with step size 0.06 and $\ell^* \in [0.2, 1.6]$ with step size 0.05. Our results are summarized in a phase diagram of Fig. 11. We see that the critical value W_c for unstable crack depends on the magnitude of ℓ^*. For larger ℓ^*, W_c is smaller because viscous dissipation plays a more negligible role during propagation. After crack initiation, the steadiness of the crack is controlled by the critical crack velocity characterized by $\ell^* \approx 1$. A fast crack ($\ell^* > 1$) propagates at steady state, in which case the crack driving force can be measured by Eq. (25). A slow crack ($\ell^* < 1$) is characterized by two characteristic non-steady behaviors; one where the crack is eventually arrested due to blunting for ($W < 0.5$), one where the crack accelerates continuously ($W > 0.5$). For both cases, G_0 cannot be determined from experiment without the use of numerical simulations since the only measurable quantity, the crack tip driving force $\mathcal{G}$, changes during the loading history and is not equal to G_0.

To the authors' knowledge, the case of crack arrest has not been systematically studied in the literature, probably due to three major reasons. First, modeling-wise, crack arrest is due to crack blunting when the deformation is very large, which cannot be captured by most existing models based on linear viscoelastic fracture. Second, experiment-wise, this phenomenon requires the need for a material formed by a single transient network with slow crack propagation velocity (i.e., high force sensitivity for chain dynamics), which imposes a strict constraint on the material system. Lastly, this phenomenon may not be observed if the specimen is not wide enough, in which case the boundary effect becomes non-negligible. As the crack propagates, the boundary effect leads to the amplification of loading rate in the region along the crack interface and increases the crack tip driving force $\mathcal{G}$. This effect is non-negligible when the sample is narrow, for instance the filament stretching experiments of complex fluids (Ligoure and Mora, 2013). In this scenario, the crack may be accelerated instead of being arrested (Ligoure and Mora, 2013; Liu et al., 2019c; Luo et al., 2014). Crack arrest may however be important in applications because fracture usually originates from very small defects. In this case, the boundary effect is negligible and

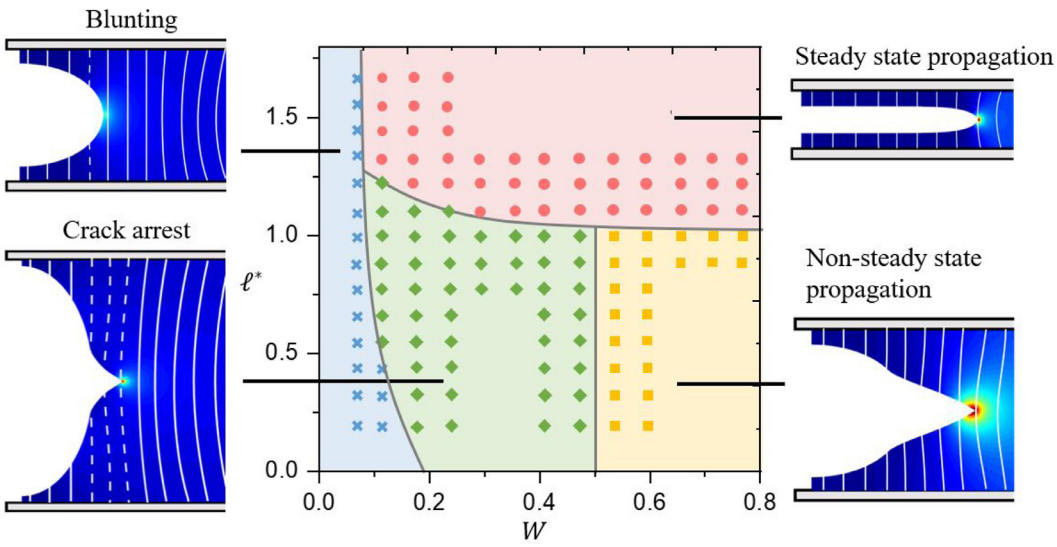

Fig. 11. A map that summarizes the four different characteristic fracture behavior of the specimen depending on the Weissenberg number $W = \dot{\epsilon}/k_d^0$ and the normalized Trumpet length $\ell^* = \ell/(L - a_0)$.

crack arrest may be an important intermediate process for material failure. One example is the debonding of an adhesive from the substrate (the probe tack test). During decohesion, the debonding mechanism transits from the interfacial crack propagation to bulk deformation (Lindner et al., 2005; Nase et al., 2008), characterized by the crack propagation-arresting process.

5. Conclusion

This work establishes a framework to study the fracture of viscoelastic materials made of transient networks. By performing an analytical study on a simple fracture problem, we identified two competitions that govern the fracture process: (a) the competition between bulk dissipation and chain deformation (measured by W), and (b) the interplay between bulk dissipation and crack propagation (measured by ℓ^*). To describe the role of bulk dissipation in fracture, we propose a loading condition where the specimen is continuously stretched by a constant true strain rate, i.e., a constant Weissenberg number W. Under this condition, our numerical experiments further determined four characteristic behaviors controlled by W and ℓ^*. For $\ell^* > 1$, the crack propagates in a steady state, for which an analytical formula was obtained to extract the intrinsic fracture toughness G_0. For $\ell^* < 1$, steady state cannot be obtained since neither external work nor bulk dissipation is negligible during propagation. In this situation, we observe an accelerating crack for $W > 0.5$ and the crack propagation-arrest phenomenon for $W < 0.5$. We note the crack propagation-arrest is caused by the interplay between chain stretch, bulk dissipation and crack blunting, which could not be studied using the linear viscoelastic fracture mechanics models. This introduces a fracture resistance mechanism where a propagating crack can be stabilized by blunting. This is also reminiscent of the interface fracture to bulk deformation transition of adhesives during the debonding process (Nase et al., 2008). For non-steady state propagation, G_0 cannot be readily calculated without performing finite element simulations because the measurable quantity $\mathcal{G}$ does not equate the intrinsic fracture energy G_0. Lastly, crack never propagates for $W \to 0$ since bulk dissipation becomes predominant and the elastic energy remains low.

This work, for the first time, evaluates the effects of network dynamics and large deformation of material on the crack driving force $\mathcal{G}$. Leveraging on this capacity, we further perform a comprehensive study on the rate-dependent fracture of viscoelastic materials at different loading conditions, and unveil the energetic mechanism behind each characteristic behavior. Our analysis shows that the effect of large deformation cannot be neglected when evaluating the crack driving force (Eq. (25)) and the combined crack propagation and blunting. As an alternative to the energy-based crack stability criterion proposed in this work, Liu et al. (2019a) recently proposed a criterion based on the local stress fields and bond damage at the tip. To unify these two approaches, future studies will seek to relate the crack driving force to the time-dependent crack tip fields near the crack. This model is developed based on brittle transient networks (Shabbir et al., 2016; Tabuteau et al., 2011; 2009) so that the network damage around the crack tip is neglected. For more general cases, the crack driving force $\mathcal{G}$ computed by Eq. (19) will include the contribution of crack tip damage. With this consideration, a characteristic length scale associated with the size of the damage zone, will arise in the problem and regulate the crack propagation (Ameli et al., 2010; Long et al., 2020). In addition, we assume here viscoelasticity is only caused by bond dynamics, while more complex rate-dependent mechanisms, e.g., chains reptation through entanglements (De Gennes, 1976; Lalitha Sridhar and

Vernerey, 2018), network-solvent interaction (Bouklas et al., 2015; Wang and Hong, 2012) and chain stiffening (Lavoie et al., 2016) are not considered. Nevertheless, the proposed framework provides a stepping-stone on which to include the above processes in future studies and generalize the model to other transient network systems including vitrimers (Röttger et al., 2017), covalent adaptable networks (CAN) (Kloxin and Bowman, 2013) and ionic hydrogels (Sun et al., 2013). More generally, the transient network theory (TNT) can also be extended to describe the rate-dependent response of a broader range of fracture resistant materials including dual-crosslink hydrogels (Mayumi et al., 2016), double-network hydrogels (Sun et al., 2012), vulcanized rubbers (Bhattacharya et al., 2011; Prabhu et al., 2013) and engineering materials such as VHB adhesive tapes (Benet et al., 2019). However, modeling the fracture of these materials requires further improvement of the model because these solids usually made of the combination of a permanent a transient network (Mayumi et al., 2013; Sun et al., 2012; 2017; Zhang et al., 2016). This leads to two competitions: (a) the energy flow in the permanent network needs to be treated separately from the transient component since it does not contribute to bulk dissipation; (b) the intrinsic fracture energy G_0 is associated with the fraction of each network and the load sharing of chains at the tip. Long and Hui (2016). A quantitative understanding of the interplay between the two networks will need to be established.

Declaration of Competing Interest

The authors declare that they have no known competing financial interests or personal relationships that could have appeared to influence the work reported in this paper.

CRediT authorship contribution statement

Tong Shen: Conceptualization, Methodology, Visualization, Investigation, Validation, Writing - original draft. **Franck J. Vernerey:** Conceptualization, Methodology, Supervision, Funding acquisition, Writing - review & editing.

Acknowledgment

FJV· gratefully acknowledges the support of the National Science Foundation under Award No. 1761918. The content is solely the responsibility of the authors and does not necessarily represent the official views of the National Science Foundation.

Appendix A. Evolution of conformation tensor $\boldsymbol{\mu}$

As discussed in Section 2, the conformation tensor $\boldsymbol{\mu}$ is obtained from averaging of chain stretch ratio $\boldsymbol{\lambda}$ over the configuration space. Let us define $\phi(\boldsymbol{\lambda})$ as the distribution of chain stretch $\boldsymbol{\lambda}$ in the configuration space, its evolution is described by the Fokker-Plank equation:

$$\frac{D\phi}{Dt} = -\boldsymbol{\nabla}\cdot(\phi\dot{\boldsymbol{\lambda}}) + r(\boldsymbol{\lambda}) \tag{26}$$

where the first term on the Right-hand side represents the contribution of elastic deformation and the second term describes the effect of inelastic processes, governed by bond dynamics in this study. If we assume affine deformation, the stretch in each chain follows the macroscopic deformation velocity gradient $\mathbf{L}$, as $\dot{\boldsymbol{\lambda}} = \mathbf{L}\boldsymbol{\lambda}$. For bond dynamics, assuming that associated chains dissociate at the current configuration ($\phi(\boldsymbol{\lambda})$) and the free chains associate in a stress free state ($\phi_0(\boldsymbol{\lambda})$), Eq. (26) can be rewritten as:

$$\frac{D\phi}{Dt} = -\mathbf{L} : (\boldsymbol{\nabla}\boldsymbol{\phi}\otimes\boldsymbol{\lambda}) - k_d\phi(\boldsymbol{\lambda}) + k_a\phi_0(\boldsymbol{\lambda}) \tag{27}$$

To obtain Eq. (4), we further multiply Eq. (27) by the dyadic $\boldsymbol{\lambda}\otimes\boldsymbol{\lambda}$ and apply the averaging operator $< \cdot >$ introduced below Eq. (3) and obtain:

$$\dot{\boldsymbol{\mu}} = \mathbf{L}\boldsymbol{\mu} + \boldsymbol{\mu}^T\mathbf{L}^T + k_a(\frac{n_t}{n} - 1)\boldsymbol{\mu}_0 - k_d\boldsymbol{\mu} \tag{28}$$

When k_a and k_d are both constants, chemical equilibrium is achieved, and the constant density of attached chains becomes $n = n_t k_a/(k_a + k_d)$. In this scenario, the above equation degenerates to Eq. (4).

Appendix B. Rate-dependent crack driving force and intrinsic fracture toughness

During the separation, the average life time of the chains bridging the crack can be defined as:

$$\bar{t} = \int_0^\infty \frac{\bar{n}}{\bar{n}_t} dt \tag{29}$$

Using Eq. (2) and assuming that $k_a \ll k_d$, the above integral can be expressed as the following exponential integral form:

$$\bar{t} = \left(\frac{f_0}{kv}\right) exp\left(\frac{f_0 k_d^0}{kv}\right) \int_{\frac{f_0 k_d^0}{kv}}^\infty \eta^{-1} exp(-\eta) d\eta \tag{30}$$

An analytical expression for the above exponential integral can be obtained when $f_0 k_d^0 / k\nu \to 0$. In this case, the average bond life time is found as:

$$\bar{t} = \left(\frac{f_0}{k\nu}\right) ln\left(\frac{k\nu}{f_0 k_d^0}\right) \tag{31}$$

Further, since the crack profile is idealized as a wedge shape with slope 1, the average length for chain dissociation is found as $\bar{\xi} = v\bar{t}$. The crack driving force $\mathcal{G}$ is then approximated as the energy needed for breaking all bridging chains at $\bar{\xi}$, i.e., $\mathcal{G} = \frac{1}{2}\overline{n}k\bar{\xi}^2$. This finally leads to the expression in Eq. (23).

Approximation of G_0: When bonds break at chemical equilibrium, the stress (σ)-distance (ξ) relation can be found from Eq. (18) as:

$$\sigma = \bar{n}_t k\xi \left[\frac{1}{1 + \frac{k_d^0}{k_a^0} exp(\frac{2k}{f_0}\xi)}\right] \tag{32}$$

This function is plotted in Fig. 12a and G_0 is evaluated by the area under this curve. To obtain an analytical approximation, this curve is approximated by an isosceles triangle characterized by the maximum stress σ_m and the corresponding stretch ξ_m. These two variables can be determined by considering $\partial\sigma/\partial\xi = 0$ as:

$$\xi_m = \frac{f_0}{2k}\mathcal{A} \quad \text{and} \quad \sigma_m = \overline{n}_t f_0 \left[\frac{\mathcal{A}}{1 + \exp(\mathcal{A})}\right] \tag{33}$$

where $\mathcal{A} = W_0(\frac{k_a^0}{k_d^0}\frac{1}{e})$ and $W_0(^*)$ is the main branch of the Lambert W function (Lambert, 1758). Eq. (22) is then calculated as the area of the triangle $G_0 = \sigma_m \xi_m$.

Appendix C. Finite element solution strategy

The finite element numerical framework is developed in our previous work (Shen et al., 2019b). Here, we introduce the solution strategy but do not detail the numerical schemes. Since the transient network theory (TNT) is developed in an incremental form, the solution strategy also takes an incremental manner. To help with the discussion, let us define Ω_s as the material domain and Γ as the boundary. At the initial state ($t = 0$), the specimen is considered at the stress-free configuration:

$$\boldsymbol{\sigma}(t = 0) = \mathbf{0} \quad \text{in} \quad \Omega_s(0). \tag{34}$$

At any time t during the simulation, the problem is solved by taking the following two steps: (i) based on the current network conformation, determine the network evolution; (ii) update the network conformation and stress.

Determine the network evolution

The network evolution is characterized by two variables: the velocity of material points $\mathbf{v}$ and the change in hydrostatic pressure $\dot{p}$, which characterizes the network evolution from kinematic and mechanical aspects, respectively. They are determined by solving for the equilibrium and incompressibility conditions in the material domain (Shen et al., 2019b):

$$\nabla \cdot \dot{\boldsymbol{\sigma}} = \mathbf{0}, \quad \text{and} \quad \nabla \cdot \mathbf{v} = 0, \quad \text{in} \quad \Omega_s \tag{35}$$

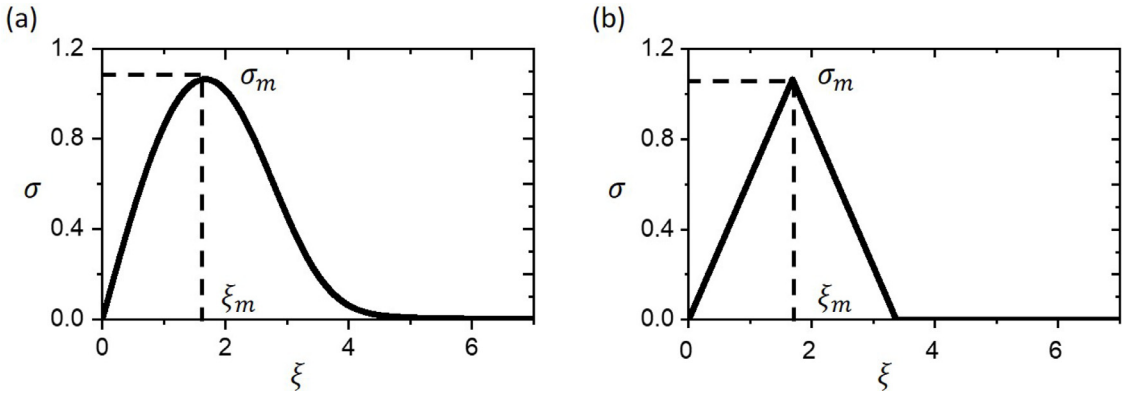

Fig. 12. (a) The $\sigma - \xi$ relation when the chains are broken at a chemical equilibrium process. (b) The approximation of $\sigma - \xi$ curve using a isosceles triangle.

the equilibrium condition is also recasted in the incremental form. The first equation can be further written as $\nabla \cdot \dot{\boldsymbol{\sigma}} = G\nabla \cdot \dot{\boldsymbol{\mu}} + \nabla \dot{p} = 0$, G being the shear modulus of material. In addition, the above equations are subjected to the velocity boundary condition:

$$\mathbf{v} = \bar{\mathbf{v}}, \quad \text{on} \quad \Gamma_D$$

where Γ_D denotes the boundary whose velocity is imposed.

Update network conformation and stress field

After $\mathbf{v}$ and $\dot{p}$ are obtained, the next step is to update the network conformation to obtain the stress fields and stored elastic energy density in the material. For this, we invoke Eq. (4) and apply an explicit time integration scheme as:

$$\begin{aligned} \boldsymbol{\mu}^{t+dt} &= \boldsymbol{\mu}^t + \dot{\boldsymbol{\mu}} dt \\ &= \boldsymbol{\mu}^t + \left[k_d\left(\boldsymbol{\mu}_0 - \boldsymbol{\mu}^t\right) + \mathbf{L}\boldsymbol{\mu}^t + \boldsymbol{\mu}^t\mathbf{L}^T\right]dt \\ p^{t+dt} &= p^t + \dot{p}^t dt \end{aligned} \tag{36}$$

where $\mathbf{L} = \nabla \mathbf{v}$ is the velocity gradient at each material point and dt is the time increment. After this, the stress and stored elastic energy density at each material point are calculated by Eqs. (6) and (5). This completes the solution at one time step. After this, the crack stability criterion is evaluated based on the stress field before proceeding to the next numerical time step.

Appendix D. Determining the stress-free height

For a pure shear test, the conformation tensor is found as $\boldsymbol{\mu} = diag\{1, \mu_{22}, \mu_{33}\}$ where μ_{22} and μ_{33} represent the mean squared stretch along the vertical and depth direction correspondingly. To obtain the stress-free configuration, we consider that the current chain state is obtained by elastically deforming the network from the stress free state. Since the deformation is elastic, it was shown in Vernerey and Long (2017) that $\boldsymbol{\mu} = \mathbf{F}\mathbf{F}^T$ where $\mathbf{F}$ is the elastic deformation gradient. Since there is no shear deformation, one can find that $\mathbf{F} = diag\{1, \sqrt{\mu_{22}}, \sqrt{\mu_{33}}$. Therefore the stress free height $H_s = H/F_{22} = H/\sqrt{\mu_{22}}$.

References

Agrawal, A., Rahbar, N., Calvert, P.D., 2013. Strong fiber-reinforced hydrogel. Acta Biomater. 9 (2), 5313–5318.

Akalp, U., Bryant, S.J., Vernerey, F.J., 2016. Tuning tissue growth with scaffold degradation in enzyme-sensitive hydrogels: a mathematical model. Soft Matter 12 (36), 7505–7520.

Ameli, A., Papini, M., Schroeder, J., Spelt, J., 2010. Fracture r-curve characterization of toughened epoxy adhesives. Eng. Fract. Mech. 77 (3), 521–534.

Benet, E., Zhu, H., Vernerey, F.J., 2019. Interplay of elastic instabilities and viscoelasticity in the finite deformation of thin membranes. Phys. Rev. E 99 (4), 42502.

Bergström, J., Boyce, M., 1998. Constitutive modeling of the large strain time-dependent behavior of elastomers. J. Mech. Phys. Solids 46 (5), 931–954.

Bhattacharya, A., Medvedev, G.A., Caruthers, J.M., 2011. Time-dependent mechanical behavior of carbon black filled elastomers. Rubber Chem. Technol. 84 (3), 296–324.

Bouklas, N., Landis, C.M., Huang, R., 2015. Effect of solvent diffusion on crack-tip fields and driving force for fracture of hydrogels. J. Appl. Mech. 82 (8).

Bryant, S.J., Vernerey, F.J., 2018. Programmable hydrogels for cell encapsulation and neotissue growth to enable personalized tissue engineering. Adv. Healthc. Mater. 7 (1), 1700605.

Chaudhury, M.K., 1999. Rate-dependent fracture at adhesive interface. J. Phys. Chem. B 103 (31), 6562–6566.

Christensen, R., 1979. A rate-dependent criterion for crack growth. Int. J. Fract. 15 (1), 3–21.

Coyle, S., Majidi, C., LeDuc, P., Hsia, K.J., 2018. Bio-inspired soft robotics: material selection, actuation, and design. Extreme Mech. Lett. 22, 51–59.

Creton, C., Ciccotti, M., 2016. Fracture and adhesion of soft materials: a review. Rep. Prog. Phys. 79 (4), 46601.

De Gennes, P., 1976. Dynamics of entangled polymer solutions. I. the rouse model. Macromolecules 9 (4), 587–593.

De Gennes, P., 1996. Soft adhesives. Langmuir 12 (19), 4497–4500.

Dhote, V., Vernerey, F.J., 2014. Mathematical model of the role of degradation on matrix development in hydrogel scaffold. Biomech. Model. Mechanobiol. 13 (1), 167–183.

Foucard, L., Aryal, A., Duddu, R., Vernerey, F., 2015. A coupled Eulerian–Lagrangian extended finite element formulation for simulating large deformations in hyperelastic media with moving free boundaries. Comput. Methods Appl. Mech. Eng. 283, 280–302. doi:10.1016/j.cma.2014.09.016.

Gent, A., 1996. Adhesion and strength of viscoelastic solids. is there a relationship between adhesion and bulk properties? Langmuir 12 (19), 4492–4496.

Ghatak, A., Vorvolakos, K., She, H., Malotky, D. L., Chaudhury, M. K., 2000. Interfacial rate processes in adhesion and friction.

Gong, J.P., Katsuyama, Y., Kurokawa, T., Osada, Y., 2003. Double-network hydrogels with extremely high mechanical strength. Adv. Mater. 15 (14), 1155–1158.

Guo, J., Hui, C.-Y., Liu, M., Zehnder, A.T., 2019. The stress field near the tip of a plane stress crack in a gel consisting of chemical and physical cross-links. Proc. R. Soc. A 475 (2227), 20180863.

Guo, J., Liu, M., Zehnder, A.T., Zhao, J., Narita, T., Creton, C., Hui, C.-Y., 2018. Fracture mechanics of a self-healing hydrogel with covalent and physical crosslinks: a numerical study. J. Mech. Phys. Solids 120, 79–95.

Haque, M.A., Kurokawa, T., Gong, J.P., 2012. Super tough double network hydrogels and their application as biomaterials. Polymer 53 (9), 1805–1822.

Holzapfel, A. G., 2000. Nonlinear solid mechanics II.

Hui, C.Y., Guo, J., Liu, M., Zehnder, A., 2019. Finite strain theory of a mode iii crack in a rate dependent gel consisting of chemical and physical cross-links. Int. J. Fract. 215 (1–2), 77–89.

Hui, C.-Y., Tang, T., Lin, Y.-Y., Chaudhury, M.K., 2004. Failure of elastomeric polymers due to rate dependent bond rupture. Langmuir 20 (14), 6052–6064.

Hui, C.-Y., Xu, D.-B., Kramer, E.J., 1992. A fracture model for a weak interface in a viscoelastic material (small scale yielding analysis). J. Appl. Phys. 72 (8), 3294–3304.

Ihsan, A.B., Sun, T.L., Kuroda, S., Haque, M.A., Kurokawa, T., Nakajima, T., Gong, J.P., 2013. A phase diagram of neutral polyampholyte–from solution to tough hydrogel. J. Mater. Chem. B 1 (36), 4555–4562.

Kloxin, C.J., Bowman, C.N., 2013. Covalent adaptable networks: smart, reconfigurable and responsive network systems. Chem. Soc. Rev. 42 (17), 7161–7173.

Knauss, W., 1966. The time dependent fracture of viscoelastic materials.

Knauss, W., 1970. Delayed failure - the griffith problem for linearly viscoelastic materials. Int. J. Fract.Mech. 6 (1), 7–20.

Knauss, W.G., 2015. A review of fracture in viscoelastic materials. Int. J. Fract. 196 (1–2), 99–146.

van der Kooij, H.M., Dussi, S., van de Kerkhof, G.T., Frijns, R.A., van der Gucht, J., Sprakel, J., 2018. Laser speckle strain imaging reveals the origin of delayed fracture in a soft solid. Sci. Adv. 4 (5), eaar1926.
Krausz, A., 1976. The theory of non-steady state fracture propagation rate. Int. J. Fract. 12 (2), 239–242.
Lake, G., Thomas, A., 1967. The strength of highly elastic materials. Proc. R. Soc. Lond. Ser.A. Math. Phys. Sci. 300 (1460), 108–119.
Lalitha Sridhar, S., Vernerey, F.J., 2018. The chain distribution tensor: linking nonlinear rheology and chain anisotropy in transient polymers. Polymers (Basel) 10 (8), 848.
Lambert, J.H., 1758. Observationes variae in mathesin puram. Acta Helvetica 3 (1), 128–168.
Lavoie, S.R., Long, R., Tang, T., 2016. An adhesive zone model for polymeric interfaces. Int. J. Fract. 197 (2), 169–183.
Li, J., Viveros, J.A., Wrue, M.H., Anthamatten, M., 2007. Shape-memory effects in polymer networks containing reversibly associating side-groups. Adv. Mater. 19 (19), 2851–2855.
Ligoure, C., Mora, S., 2013. Fractures in complex fluids: the case of transient networks. Rheol. Acta 52 (2), 91–114.
Lin, S., Yuk, H., Zhang, T., Parada, G.A., Koo, H., Yu, C., Zhao, X., 2016. Stretchable hydrogel electronics and devices. Adv. Mater. 28 (22), 4497–4505.
Lindner, A., Derks, D., Shelley, M., 2005. Stretch flow of thin layers of Newtonian liquids: fingering patterns and lifting forces. Phys. Fluids 17 (7), 72107.
Liu, M., Guo, J., Hui, C.-Y., Zehnder, A., 2019a. Crack tip stress based kinetic fracture model of a pva dual-crosslink hydrogel. Extreme Mech. Lett. 29, 100457.
Liu, M., Guo, J., Li, Z., Hui, C.-Y., Zehnder, A.T., 2019b. Crack propagation in a pva dual-crosslink hydrogel: crack tip fields measured using digital image correlation. Mech. Mater. 138, 103158.
Liu, M., Guo, J., Li, Z., Hui, C.-Y., Zehnder, A.T., 2019c. Crack propagation in a pva dual-crosslink hydrogel: crack tip fields measured using digital image correlation. Mech. Mater. 138, 103158.
Long, R., Hui, C.-Y., 2015. Crack tip fields in soft elastic solids subjected to large quasi-static deformation a review. Extreme Mech. Lett. 4, 131–155.
Long, R., Hui, C.-Y., 2016. Fracture toughness of hydrogels: measurement and interpretation. Soft Matter 12 (39), 8069–8086.
Long, R., Hui, C.-Y., Gong, J. P., Bouchbinder, E., 2020. The fracture of highly deformable soft materials: atale of two length scales. arXiv preprint arXiv:2004.03159.
Long, R., Mayumi, K., Creton, C., Narita, T., Hui, C.-Y., 2014. Time dependent behavior of a dual cross-link self-healing gel: theory and experiments. Macromolecules 47 (20), 7243–7250.
Luo, F., Sun, T.L., Nakajima, T., Kurokawa, T., Zhao, Y., Ihsan, A.B., Guo, H.L., Li, X.F., Gong, J.P., 2014. Crack blunting and advancing behaviors of tough and self-healing polyampholyte hydrogel. Macromolecules 47 (17), 6037–6046.
Mao, Y., Lin, S., Zhao, X., Anand, L., 2017. A large deformation viscoelastic model for double-network hydrogels. J. Mech. Phys. Solids 100, 103–130.
Mayumi, K., Guo, J., Narita, T., Hui, C.Y., Creton, C., 2016. Fracture of dual crosslink gels with permanent and transient crosslinks. Extreme Mech. Lett. 6, 52–59.
Mayumi, K., Marcellan, A., Ducouret, G., Creton, C., Narita, T., 2013. Stress–strain relationship of highly stretchable dual cross-link gels: separability of strain and time effect. ACS Macro Lett. 2 (12), 1065–1068.
Millereau, P., Ducrot, E., Clough, J.M., Wiseman, M.E., Brown, H.R., Sijbesma, R.P., Creton, C., 2018. Mechanics of elastomeric molecular composites. Proc. Natl. Acad. Sci. 115 (37), 9110–9115.
Moutos, F.T., Freed, L.E., Guilak, F., 2007. A biomimetic three-dimensional woven composite scaffold for functional tissue engineering of cartilage. Nat. Mater. 6 (2), 162.
Narita, T., Mayumi, K., Ducouret, G., Hebraud, P., 2013. Viscoelastic properties of poly (vinyl alcohol) hydrogels having permanent and transient cross-links studied by microrheology, classical rheometry, and dynamic light scattering. Macromolecules 46 (10), 4174–4183.
Nase, J., Lindner, A., Creton, C., 2008. Pattern formation during deformation of a confined viscoelastic layer: from a viscous liquid to a soft elastic solid. Phys. Rev. Lett. 101 (7), 74503.
Pellens, L., Ahn, K.H., Lee, S.J., Mewis, J., 2004. Evaluation of a transient network model for telechelic associative polymers. J. Nonnewton Fluid Mech. 121 (2–3), 87–100.
Prabhu, R., Klitkou, R., Medvedev, G.A., Caruthers, J.M., 2013. A critical analysis of the effect of crosslinking on the linear viscoelastic behavior of styrene–butadiene rubber and other elastomers. J. Polym. Sci. Part B: Polym. Phys. 51 (8), 687–697.
Qi, Y., Zou, Z., Xiao, J., Long, R., 2019. Mapping the nonlinear crack tip deformation field in soft elastomer with a particle tracking method. J. Mech. Phys. Solids 125, 326–346.
Röttger, M., Domenech, T., van der Weegen, R., Breuillac, A., Nicolaÿ, R., Leibler, L., 2017. High-performance vitrimers from commodity thermoplastics through dioxaborolane metathesis. Science 356 (6333), 62–65.
Saulnier, F., Ondarçuhu, T., Aradian, A., Raphaël, E., 2004. Adhesion between a viscoelastic material and a solid surface. Macromolecules 37 (3), 1067–1075.
Schapery, R.A., 1975. A theory of crack initiation and growth in viscoelastic media. Int. J. Fract. 11 (1), 141–159.
Schapery, R.A., 1984. Correspondence principles and a generalizedj integral for large deformation and fracture analysis of viscoelastic media. Int. J. Fract. 25 (3), 195–223.
Shabbir, A., Huang, Q., Chen, Q., Colby, R.H., Alvarez, N.J., Hassager, O., 2016. Brittle fracture in associative polymers: the case of ionomer melts. Soft Matter 12 (36), 7606–7612.
Shen, T., Benet, E., Sridhar, S.L., Abadie, J., Piat, E., Vernerey, F.J., 2019a. Separating the contributions of zona pellucida and cytoplasm in the viscoelastic response of human oocytes. Acta Biomater. 85, 253–262.
Shen, T., Long, R., Vernerey, F., 2019b. Computational modeling of the large deformation and flow of viscoelastic polymers. Comput. Mech. 63 (4), 725–745.
Sun, J.-Y., Zhao, X., Illeperuma, W.R., Chaudhuri, O., Oh, K.H., Mooney, D.J., Vlassak, J.J., Suo, Z., 2012. Highly stretchable and tough hydrogels. Nature 489 (7414), 133.
Sun, T.L., Kurokawa, T., Kuroda, S., Ihsan, A.B., Akasaki, T., Sato, K., Haque, M.A., Nakajima, T., Gong, J.P., 2013. Physical hydrogels composed of polyampholytes demonstrate high toughness and viscoelasticity. Nat. Mater. 12 (10), 932–937.
Sun, T.L., Luo, F., Hong, W., Cui, K., Huang, Y., Zhang, H.J., King, D.R., Kurokawa, T., Nakajima, T., Gong, J.P., 2017. Bulk energy dissipation mechanism for the fracture of tough and self-healing hydrogels. Macromolecules 50 (7), 2923–2931.
Tabuteau, H., Mora, S., Ciccotti, M., Hui, C.-Y., Ligoure, C., 2011. Propagation of a brittle fracture in a viscoelastic fluid. Soft Matter 7 (19), 9474–9483.
Tabuteau, H., Mora, S., Porte, G., Abkarian, M., Ligoure, C., 2009. Microscopic mechanisms of the brittleness of viscoelastic fluids. Phys. Rev. Lett. 102 (15), 155501.
Tanaka, F., Edwards, S., 1992. Viscoelastic properties of physically crosslinked networks. 1. transient network theory. Macromolecules 25 (5), 1516–1523.
Tobolsky, A., Eyring, H., 1943. Mechanical properties of polymeric materials. J. Chem. Phys. 11 (3), 125–134.
Vernerey, F., Long, R., Brighenti, R., 2017. A statistically-based continuum theory for polymers with transient networks. J. Mech. Phys. Solids 107, 1–20. doi:10.1016/j.jmps.2017.05.016.
Vernerey, F.J., 2018. Transient response of nonlinear polymer networks: akinetic theory. J. Mech. Phys. Solids 115, 230–247.
Vernerey, F.J., Brighenti, R., Long, R., Shen, T., 2018a. Statistical damage mechanics of polymer networks. Macromolecules 51 (17), 6609–6622.
Vernerey, F.J., Shen, T., Sridhar, S.L., Wagner, R.J., 2018b. How do fire ants control the rheology of their aggregations? A statistical mechanics approach. J. R. Soc. Interface 15 (147), 20180642.
Wang, X., Hong, W., 2012. Delayed fracture in gels. Soft Matter 8 (31), 8171–8178.
Williams, M., 1968. The kinetic energy contribution to fracture propagation in a linearly viscoelastic material. Int. J. Fract. Mech. 4 (1), 69–78.
Wu, J., Cai, L.-H., Weitz, D.A., 2017. Tough self-healing elastomers by molecular enforced integration of covalent and reversible networks. Adv. Mater. 29 (38), 1702616.
Yamamoto, M., 1956. The visco-elastic properties of network structure I. General formalism. J. Phys. Soc. Jpn. 11 (4), 413–421.
Yu, K., Xin, A., Wang, Q., 2018. Mechanics of self-healing polymer networks crosslinked by dynamic bonds. J. Mech. Phys. Solids 121, 409–431.

Zehnder, A.T., 2012. Energy flows in elastic fracture. In: Fracture Mechanics. Springer, pp. 33–54.
Zhang, H.J., Sun, T.L., Zhang, A.K., Ikura, Y., Nakajima, T., Nonoyama, T., Kurokawa, T., Ito, O., Ishitobi, H., Gong, J.P., 2016. Tough physical double-network hydrogels based on amphiphilic triblock copolymers. Adv. Mater. 28 (24), 4884–4890.
Zhao, X., 2014. Multi-scale multi-mechanism design of tough hydrogels: building dissipation into stretchy networks. Soft Matter 10 (5), 672–687.